Contour interpolation by vector-field combination

Carlo Fantoni
Department of Psychology, BRAIN Center for Neuroscience, University of Trieste, Trieste, Italy

Walter Gerbino
Department of Psychology, BRAIN Center for Neuroscience, University of Trieste, Trieste, Italy

We model the visual interpolation of missing contours by extending contour fragments under a smoothness constraint. Interpolated trajectories result from an algorithm that computes the vector sum of two fields corresponding to different unification factors: the good continuation (GC) field and the minimal path (MP) field. As the distance from terminators increases, the GC field decreases and the MP field increases. Viewer-independent and viewer-dependent variables modulate GC-MP contrast (i.e., the relative strength of GC and MP maximum vector magnitudes). Viewer-independent variables include the local geometry as well as more global properties such as contour support ratio and shape regularity. Viewer-dependent variables include the retinal gap between contour endpoints and the retinal orientation of their stems. GC-MP contrast is the only free parameter of our field model. In the case of partially occluded angles, interpolated trajectories become flatter as GC-MP contrast decreases. Once GC-MP contrast is set to a specific value, derived from empirical measures on a given configuration, the model predicts all interpolation trajectories corresponding to different types of occlusion of the same angle. Model predictions fit psychophysical data on the effects of viewer-independent and viewer-dependent variables.

Keywords: interpolation, amodal completion, simulation, good continuation, minimum principle, smoothness, model

Introduction

Human observers can overcome the fragmentation of the optic input and perceive shapes partially specified by image contours. One can distinguish three cases of perceptual integration of optic fragments:

- *virtual lines* perceived as the most natural chaining of isolated dots (Kanizsa, 1979) or oriented elements (Kovàcs & Julesz, 1993; Field, Hayes, & Hess, 1993; Kovàcs, 1996);
- *amodal* contours of partially occluded shapes, typically defined by T-junction stems (Bregman, 1981; Kanizsa & Gerbino, 1982; Nakayama, Shimojo & Silverman, 1989);
- *modal* contours perceived in Kanizsa's illusory figures, as well as in two-dimensional (2D) (Gulick & Lawson, 1976) and three-dimensional (3D) (Grimson, 1981) random-dot stereograms.

These three cases involve increasing degrees of phenomenal presence of unitary shapes. In virtual groupings, implicit lines connect parts perceived as separate elements. In amodal completion, image-specified contours are not only perceptually grouped; they also continue behind occluders along trajectories that bound a partially occluded surface. Modal completions are characterized by the visibility of illusory contours that bound a perceptually integrated surface.

Virtual, amodal, and modal integrations share common geometric aspects, implicit in models such as the Boundary Contour System (Grossberg & Mingolla, 1985; Kelly & Grossberg, 2000) and made explicit in the identity hypothesis (Shipley & Kellman, 1992a). The shape of interpolated contours can reveal how contextual variables, such as scale, orientation, support ratio (the proportion of image-specified contours), and global shape, act when the local stimulation is weak or absent (Koffka, 1935, pp. 140-147).

Such ideas capture an important distinction between the shape of the trajectory that interpolates contour fragments and its phenomenal salience. In accordance with the identity hypothesis, we assume the shape of the trajectory is the output of a general-purpose visual interpolation (VI) process; i.e., of a shape integrator activated in all cases of missing local information (for instance, because of occlusion). The shape integrator is analogous to the 3D-shape modeler discussed by Adelson and Pentland (1996) in their "workshop metaphor" of visual processing. On the other hand, the degree of salience of interpolated parts might be explained in different ways, depending on the theoretical approach to VI.

According to a two-stage approach (Takeichi, Nakazawa, Murakami, & Shimojo, 1995; Kellman, Guttman, & Wickens, 2001), the decision to interpolate is taken at the end of a first stage in which the input is analyzed to evaluate its compatibility with geometric constraints. If the input is geometrically compatible, optic fragments are fed to the shape integrator that generates

DOI 10:1167/3.4.4 Received September 19, 2001; published May 29, 2003 ISSN 1534-7362

the interpolated trajectory in the second stage. According to this approach, the trajectory is immaterial to the compatibility analysis performed in the first stage. However, the degree of salience might be the output of the first stage (reflecting the amount of compatibility between stimulus properties and geometric constraints), the second stage (reflecting metrical aspects of the interpolated shape such as curvature, length, and number of inflections), or both.

According to a dynamic approach, optic fragments represent the stimulus conditions for a completion process whose final state can achieve a variable degree of stability. The degree of stability determines the phenomenal salience of the interpolated shape. Salience is correlated with (not caused by) compatibility and metrical aspects. In this case, both salience and compatibility derive from the dynamic constraints of the interpolation process.

Most VI models adopt a two-stage approach and are focused on geometric compatibility constraints. Some interpolation solutions generated by such models do not appear adequately justified on theoretical grounds (Witkin & Tenenbaum, 1983).

Our VI model is consistent with the dynamic approach and with the general idea that perceptual completions reflect organization according to the minimum principle (Koffka, 1935; Buffart, Leeuwenberg, & Restle, 1981; Kanizsa & Gerbino, 1982; Hatfield & Epstein, 1985). The minimum principle is embodied in both structural and metrical aspects of perceptual integration.

Figure 1. Two prototypical kinds of amodal completion behind black occluders. In a, a single concave region is amodally completed and perceived as a partially occluded convex form. In b, three convex regions are amodally unified and perceived as a single partially occluded form.

Consider amodal completion of partially occluded angles. Amodally completed shapes perceived in Figure 1 correspond to groupings that are structurally different from the mosaic of image regions. The superiority of completion over mosaic interpretations is consistent with a tendency to minimize form complexity (Figure 1a) or object numerosity (Figure 1b). Locally, completions are supported by the segregation of T-junction stems from T-junction tops. Paired stems become the visible portions of the partially occluded contour, whereas tops belong to the contour of the occluding surface.

However, the phenomenology of amodal completion indicates that image contours are not only grouped or chained. They are perceptually interpolated by a smooth curve, different from the sharp-vertex angle resulting from the simple extrapolation of T-junction stems. The smooth amodal trajectory is consistent with a tendency to minimize metrical parameters, such as curvature and length. The shape and salience of an interpolated trajectory can be evaluated in psychophysical experiments using procedures such as probe localization and magnitude estimation (Takeichi, 1995; Kellman, Shipley, & Kim, 1996; Fantoni, 2000; Gerbino & Fantoni, 2000; Kellman, Temesvary, Palmer, & Shipley, 2000; Fantoni & Gerbino, 2001). Similar methods have been used to evaluate virtual and modal contour integrations (Dumais & Bradley, 1976; Kellman & Shipley, 1991; Hon, Maloney, & Landy, 1997).

Previous VI models did not explain how viewer-independent and viewer-dependent variables interact and determine the shape of interpolated contours. Viewer-independent variables include figural properties such as positions and relative orientations of fragments, shape regularity, and support ratio. Viewer-dependent variables include retinal size and orientation of the image.

Following a dynamic, Gestalt-oriented approach, we modeled VI as the product of two context-sensitive forces corresponding to two classical factors of organization, good continuation (GC) and minimal path (MP). Given two contour fragments, GC predicts that extrapolations minimize the variation of curvature of each fragment, whereas MP predicts that endpoints are connected along the minimum-length trajectory. The effects of various contextual variables on interpolation trajectories are reduced to variations of a unique parameter, GC-MP contrast, that describes the relative strength of GC and MP vectors (Equation 1).

$$GC\text{-}MP\ contrast = \frac{GC - MP}{GC + MP} \quad (1)$$

For any given GC-MP contrast, our model generates a unique interpolation solution that represents a compromise between GC and MP. In the workshop-metaphor language, the interpolator finds a trajectory that connects the two input fragments by keeping the total cost of deviating from both GC and MP at a minimum (Adelson & Pentland, 1996).

The currently implemented algorithm generates trajectories by iteratively computing a series of GC- and MP-vector sums associated to convergent rectilinear fragments. The algorithm provides solutions for the completion of partially specified angles (link to simulator).

Angle completion is relevant for several reasons:

- The interpolated trajectory can be estimated by using a simple psychophysical task in which observers are required to locate differently oriented probes tangent to the partially specified contour. The application of the probe localization technique is straightforward in the angle completion case, when an interpolated trajectory without inflections is possible. It is less obvious when one or more inflections are necessary.
- The sharp vertex is a unique geometric solution that can be contrasted with data consistent with smooth monotonic interpolations (Takeichi, 1995; Fantoni & Gerbino, 2001). When one or more inflections are necessary, there is no unique geometric solution to be contrasted with model-based trajectories consistent with empirical estimates.
- In the sharp-vertex case, the smoothness constraint embodied in our field model can be tested empirically. A smooth curve can be fitted to tangents positioned by observers and compared to the corresponding rectilinear angle.

The discrepancy between the sharp-vertex solution and model-based predictions provides a compact parameter of the interpolation trajectory, which facilitates the comparison of contrasting models.

Geometric Compatibility Criteria

Most VI theories and models assume that compatibility of unconnected fragments with geometric constraints is a condition for the activation of the interpolation routine (Shipley & Kellman, 2001). A typical geometric constraint regards the amplitude of the interpolation angle bounded by GC extrapolations.

Kellman and Shipley (1991) hypothesized that the visual system interpolates image fragments only if they are relatable; i.e., if their linear extensions intersect and form an interpolation angle between 90° (minimal relatability) and 180° (collinearity or perfect relatability). Kellman and Shipley (1991, p. 180) also demonstrated that VI strength increases as the interpolation angle increases from 90° to 180°.

Singh and Hoffman (1999) suggested that the definition of relatability should be reformulated to make it consistent with two constraints: viewpoint genericity and extended gradedness. Viewpoint genericity implies the rejection of unstable interpolated paths that would be contradicted by minimal displacements of the viewpoint. Extended gradedness relates VI strength not only to the size of the interpolation angle (already considered by Kellman & Shipley, 1991) but also to the offset between parallel image segments. Singh and Hoffman's reformulation agrees with the hypothesis that the critical VI criterion is the number of inflections in the interpolated path (Takeichi et al., 1995).

Independent of the specific formulation, relatability is the fundamental component of a two-stage theory of contour interpolation, centered on T-junction stems as sources of local information about partial occlusion. However, the role of T-junctions and the choice of the most adequate level of analysis (contours, surfaces, or volumes) are controversial.

Tse (1999a, 1999b) argued that when contextual information about occlusion is available, image fragments are amodally completed if they can merge into a single volume, irrespective of image-contour relatability. Volume mergeability does not rely on T-junctions.

Tse rejected the hypothesis that contour interpolation occurs if and only if two relatable T-junction stems are present in the image. However, this condition qualifies an extreme version of a contour-based VI theory. For instance, Figure 2 is compatible with a contour-based theory that tolerates the existence of implicit T-junctions. The presence of relatable T-junction stems should be considered as a facilitating, not a necessary, condition that usually cooperates with the similarity of surface properties (color, texture, orientation, and motion).

Tse (1999a, in particular his Figure 2b) emphasized that relatability is not a sufficient condition either. Collinear segments can become parts of different wholes if other factors, typically similarity and closure, prevail. However, this is true of all Gestalt-like factors, whose organizational effects depend on their relative strengths (Wertheimer, 1923).

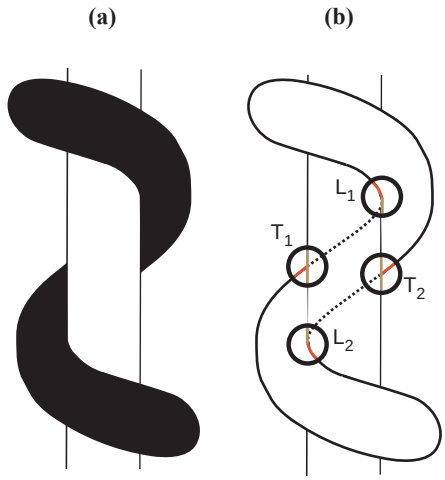

Figure 2. A Tse-like demonstration. In a, two separated regions are amodally completed into a partially occluded worm despite the lack of corresponding T-junction stems. In b, the T_1-junction stem is unified with a segment of L_1 and the T_2-junction stem with a segment of L_2. The juxtaposition of concave and convex solids can lead to image singularities in which T-junctions degenerate into L-junctions.

Given that relatability can be generalized to the 3D domain (Kellman, 2000), its difference from Tse's mergeability is not one of geometric dimensionality. Such

notions differ because relatability rejects noncollinear parallel fragments, whereas mergeability allows their interpolation. In our view, Singh and Hoffman's reformulation of relatability is fully consistent with Tse's mergeability.

Both relatability and mergeability are proposed as a priori geometric notions, used as decision criteria for entering the interpolation stage. On the contrary, dynamic models such as ours derive compatibility constraints from the properties of the interpolation process. Assumptions about the directions of completion forces and their decay functions determine the range of input fragments compatible with valid model-based solutions.

To summarize, our model has two goals: to predict precise interpolation trajectories based on general principles of organization and to define dynamic compatibility criteria based on properties of the final configuration. The section on our field model will include the discussion of dynamic compatibility criteria for rectilinear and curvilinear fragment pairs.

Weak and Strong VI Models

We suggest a distinction between models that simply identify the necessary and sufficient conditions for relatability or mergeability without predicting the metrical aspect of the interpolated trajectory (weak VI models) and models that predict the shape of the interpolated trajectory (strong VI models).

Strong VI models recommend themselves on two grounds: they generate quantitative predictions and can be easily falsified; and, they can account for subtle differences between amodal trajectories revealed by psychophysical measurements.

Strong models of contour interpolation map input fragments into output lines that include amodal trajectories described by an interpolating function. An oriented minimal-length fragment is defined as an edgel, an edge element with only one endpoint. An edgel pair includes two edgels specified by endpoint positions and by their relative orientation.

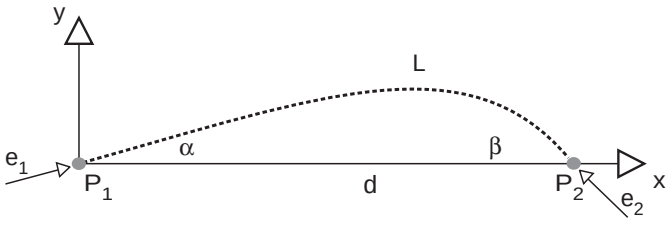

Figure 3. Two generic relatable edgels (P_1, α) and (P_2, β). The dotted line of length L is a perceptually plausible interpolation of the two edgels.

Figure 3 illustrates the generic case of two nonparallel edgels, e_1 and e_2, with endpoints in P_1 and P_2 ($P_1, P_2 \in \mathbf{R}^2$), and orientations $\alpha \neq \beta$ ($\alpha, \beta \in \{0\text{-}360°\}$) relative to the straight connecting line through P_1 and P_2, such that their extrapolations converge toward an asymmetric vertex. The two edgels are separated by $d = |P_2\text{-}P_1|$. The dotted line represents a perceptually plausible interpolation of length L.

Interpolation Models

Despite the amount of evidence on constraining factors, the shape of the visually interpolated trajectory remains controversial. Applied mathematics and computational theory provide several methods for connecting a set of fragments by good-looking curves. Other hypotheses derive from research in human vision.

In this section, we review 10 models that propose specific VI processes. All models make predictions for nontrivial configurations in which fragments, pacman sides or T-junction stems, do not lie on a straight line and their linear extrapolations form an interpolation angle $\theta \neq 0$ (where $\theta = 180° - \alpha - \beta$). Some models belong to a common framework, defined by the use of the elastica functional as a reference parameter for identifying the interpolation trajectory that minimizes the total curvature.

Elastica Models

The problem of finding the plane curve L, which minimizes the total squared curvature along a path that connects two oriented elements, was first introduced in the field of differential geometry by Euler in 1744 (Mumford, 1994). Such curves have been named elastica. The problem of elasticity has been rediscovered by Love (1927) and other mathematicians (Birkhoff, Burchard, & Thomas, 1965; Bryant & Griffiths, 1986).

In computer vision, Horn (1981) was the first to introduce the elastica functional Γ_{el} as the criterion for selecting a smooth curve connecting two edgels. Weiss (1988) proposed a scale-invariant version described by the following equation:

$$\Gamma_{el}(\psi) \overset{def}{=} L\int_0^L k(s)^2\, ds \qquad (2)$$

where $0<s<L$ is the arc length along the curve denoted by its orientation representation as $\psi(s)$, and the curvature of the curve at s is given by

$$k(s) = \frac{d\psi(s)}{ds} . \qquad (3)$$

Mumford (1994) proposed to utilize the elastica for finding the best interpolating curve in amodal completion. Their elastica functional, slightly different from the one by Weiss, is:

$$\Gamma_{el}(\psi) \overset{def}{=} \int_0^L (\eta_1 k(s)^2 + \eta_2)\, ds \qquad (4)$$

where η_1 and η_2 are constants.

Mumford (1994) modeled elastica by implementing a stochastic process of Brownian diffusion from one edgel

toward the other, similar to the stochastic completion field by Williams and Jacobs (1997). Curvatures of diffusion path are normally distributed, so that once integrated the tangent direction is a Brownian motion (Mumford, 1994, p. 495).

No analytic expression is known to calculate the shape of the curve that minimizes the elastica functional. Sharon, Brandt, and Basri (1997) proposed an approximation allowing them to derive specific trajectories as a function of angles α and β. Figure 4 shows the trajectory predicted by such an approximation when $\alpha = 80°$ and $\beta = 20°$.

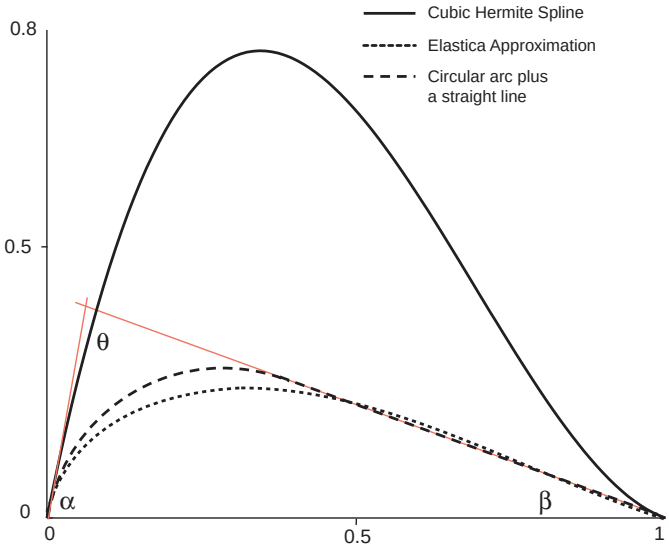

Figure 4. Different interpolations of the two edgels with orientations $\alpha = 80°$ and $\beta = 20°$. In the proximity of a large angle, the cubic Hermite spline (solid line) follows the tangent to the corresponding edgel, whereas the elastica (dotted line) accumulates a high curvature and behaves like the combination of circular arc plus a straight segment (dashed line). When the $(\alpha - \beta)$ difference is large, both the cubic Hermite spline and this elastica approximation lie outside the rectilinear angle defined by GC extrapolations. The trajectory of the elastica displayed here has been adapted from Sharon et al. (1997, Figure 2b).

Spline Models

Spline models interpolate at least two edgels by a smooth curve that minimizes the total bending energy by joining piecewise polynomials of low degree. Spline functions have been used to predict amodal and modal trajectories in 2D and 3D interpolations (Williams & Hanson 1996; Williams, 1997).

Sharon et al. (1997) demonstrated that a cubic Hermite spline is a good approximation of elastica when the deviation of edgel orientations from the straight connecting line is small. However, for large (α, β) angles, the elastica accumulates a high curvature at each end whereas the spline continues to follow the tangent to the two elements at both ends. As shown in Figure 4, the spline that connects fragments with a large $(\alpha - \beta)$ difference is still a good-looking curve, but quite different from the elastica curve approximated by Sharon et al.

Ullman's Network Model

Ullman (1976) was the first to apply a method that approximates a spline of least energy to 2D completion. He developed a network model to fill in gaps and to predict the trajectory of modal illusory contours. Ullman's network generates pairs of circular arcs tangent to edgels and to each other; then it selects the arc pair that minimizes the total bending energy.

Guy and Medioni Tensor Voting Model

Guy and Medioni (1996) extended Ullman's model to include the generation of trajectories with variable local curvature. The smooth joining of two circular arcs, proposed by Ullman, cannot generate elliptical trajectories. To account for the generation of elliptical trajectories, Guy and Medioni's model utilizes the joining of an unlimited number of local circular arcs. Every site (i.e., a pixel or edgel located in an image gap) receives a set of votes from every fragment of the intensity image. Votes include information about the relative orientation and strength of the site.

Guy and Medioni's model generates a distribution of interpolation trajectory (IT) with different strengths by superposing votes from all active sites (i.e., fragments or dots) and computing measures of orientation agreement. The IT uncertainty distribution is represented by "the best fit ellipse representing the moments of those votes" (Guy & Medioni, 1996, p. 13).

Note that Guy and Medioni's model does not predict any variation of IT's shape as a function of proximity between edge elements. Each extension field (the "maximum likelihood directional vector field describing the contribution of a single unit-length edge element to its neighborhood in terms of length and direction," p. 8) is invariant with respect to proximity; i.e., it is always circular.

Kellman and Shipley's Monotonic Curve Model

Kellman and Shipley (1991) not only described geometric constraints for contour relatability. They proposed an interpolation model slightly different from the one embodied in Ullman's network but always based on the circular arc as a geometric primitive. One circular arc is sufficient for connecting a pair of convergent symmetric fragments (i.e., mirror-oriented edgels, equidistant from the straight-line vertex). Convergent asymmetric fragments are interpolated by a circular arc plus a straight segment that connects such an arc with the far edgel (Figure 4). The straight segment compensates the figural asymmetry.

Kellman and Shipley's interpolation model combines smooth closure, represented by the circular path, and

good continuation, represented by the straight line, to form a good-looking monotonic connection.

Stochastic Completion Field Model

Suppose that edgels emit particles that follow Brownian trajectories and produce a stochastic completion field (Mumford, 1994; Williams & Jacobs, 1997; Thornber & Williams, 1999). The most likely path taken by a particle in the stochastic field is similar to the curve of least energy, according to the elastica energy functional (Thornber & Williams, 1996; Williams & Jacobs, 1997).

Thornber and Williams (1999) characterized the completion of angles using a mixture of stochastic processes. According to their model, the most likely trajectory results from the combination of random impulses drawn from a mixture of two limiting distributions: one consisting of weak but frequently acting impulses (Gaussian limit), the other of strong but infrequently acting impulses (Poisson limit). As an effect of a random combination, particles tend to travel in smooth, short paths characterized by occasional orientation discontinuities.

Such an approach is limited by the different roles of the two endpoints (source vs. sink), the unidirectional computation of trajectories (from source to sink), and the computational cost of generating a population of trajectories.

Snake Model

The snake model is an active contour model using "an energy minimizing spline guided by external constraint forces and influenced by image forces that pull it toward features such as lines and edges" (Kass, Witkin, & Terzopolous, 1987). At the 3D level, the snake acts like a balloon. Its final shape results from the minimization of internal and external energies. The internal energy is defined by the equation:

$$E_{\text{int}} = \frac{1}{2}\int \alpha\left|v_{xx}(s)\right|^2 + \beta\left|v_x(s)\right|^2 ds \qquad (5)$$

where v_{xx} and v_x are approximations of the first and second derivatives.

The $v_{xx}(s)^2$ plays the role of $k(s)^2$ in the Mumford's elastica functional (Equation 4). Therefore the snake energy and the elastica functional differ primarily in their second term: the snake minimizes $v_{xx}(s)^2$, whereas the elastica minimizes the arc length. However, the significance of such a difference is unclear.

Grimson's Model

Grimson (1981) proposed a model based on the application of the "no news is good news" principle to the interpolation of 2D contours and 3D surfaces. The principle states that the absence of local information on an abrupt change of curvature (because of partial occlusion or input fragmentation) specifies surface smoothness. In the 2D domain, the contour that minimizes the quadratic variation is the most consistent with such a principle. Grimson's model has been embodied by Marr (1982) in his general approach to interpolation.

Singh and Hoffman's Model

Singh and Hoffman (1999) proposed that interpolation depends on the minimization of of both curvature variability and total turning (integral of the absolute value of curvature along the IT). A spline of least energy and a strength measure based on inflections are the implications of their model.

Heitger and von der Heydt's Ortho-Para Model

Heitger, von der Heydt, Peterhans, Rosenthaler, and Kübler (1998) developed a computational model of end-stopped-cell extrapolations originally proposed by Heitger and von der Heydt (1993). The model accounts for the curvilinear shape of modal interpolations perceived in Ehrenstein and Kanizsa's illusory figures. Contour trajectories depend on ortho and para grouping fields. Illusory contours in line-ending displays depend on the ortho grouping of activations transversal to line directions. Illusory contours in pacman displays depend on the para grouping of activations generated by the relatable sides of two pacman concavities.

Notice that the activation of the two fields considered by Heitger et al. (1998) is qualitatively different from the combination of GC and MP fields used in our model to obtain a compromise trajectory. Ortho and para grouping fields do not interact, each completing a different part of the fragmented image. For instance, in pacman displays, the ortho field supports the completion of partially occluded circles, whereas the para field supports the completion of the illusory occluder.

A Comparison of Previous Interpolation Models

Taken together, the above-reviewed models represent a major attempt of providing specific solutions for the recovery of missing contours. Despite important differences, they share common features. They are all based on local information and embody a preference for the smoothest solution. However, as pointed out by Witkin and Tenenbaum (1983), measures of smoothness depend on the choice of parameters to be minimized. The arbitrariness of such a choice is consistent with the general notion that the minimum principle does not provide unique solutions (Gerbino, 2001) and with the possibility that, in a given situation, different and independent minimization processes interact.

On a practical level, previous models, though formally different, often make similar predictions. For instance, they interpolate convergent symmetric fragments, both rectilinear (like those in Figure 1) and circular (like those in Figure 17), by a circular arc or by curves that closely approximate it. Though generated by

analytically different functions (circle, cubic spline) or by different algorithms, such trajectories are almost indistinguishable. To evaluate the differential predictive value of models, one should consider convergent asymmetric fragments (like those in Figure 10) and other patterns.

Table 1 provides a synthetic comparison of predictions derived from various strong VI models. Cells contain information about sensitivity (**S**) or invariance (**I**) of trajectories predicted by specific models (column) with respect to given stimulus features (rows). All models considered in Table 1 generate interpolated trajectories sensitive to occlusion asymmetry (i.e., to the difference between the two angles defined by GC and MP lines), a feature not included in the table.

As summarized in Table 1, trajectories predicted by previous models depend on local variables defining the interpolation angle (relative position and orientation of fragments), but not on contextual variations (changes of scale, orientation, contour polarity, and global shape regularity). The sensitivity to support ratio is a distinguishing feature of some models. The insensitivity to global properties and viewing conditions may be considered as a desirable feature of trajectories interpolated by an ideal mechanism focused on target properties.

Table 1. A Synthetic Comparison of Predictions Derived From Various Strong VI Models

	Spline model Ullman (1976) Kellman & Shipley (1991)	Stochastic model Snake model Guy & Medioni (1999)	Field model
Interpolation angle	S	S	S
Support ratio	I	S	S
Retinal gap, Orientation, Contour polarity, Shape regularity	I	I	S

Models can be evaluated by considering the sensitivity (S) or invariance (I) of predicted interpolation trajectories with respect to local and contextual variables.

However, psychophysical evidence on human vision runs against interpolation invariance. Trajectories interpolated by human observers are sensitive to the following contextual variations:

Scale. Take a diamond with vertices partially occluded by four disks and make it contract and expand rigidly, so that support ratio remains constant. As the retinal gap between line-endings decreases, amodally completed angles appear increasingly flattened, making the partially occluded diamond more and more similar to a disk. Fantoni and Gerbino (2002) compared different events in which the retinal gap subtended a 3.5° angle at the point of maximum expansion and a variable angle at the point of maximum contraction. Observers were required to estimate the perceived roundness of the occluded shape at the point of maximum contraction. Figure 5 shows roundness estimates as a function of minimum retinal gap.

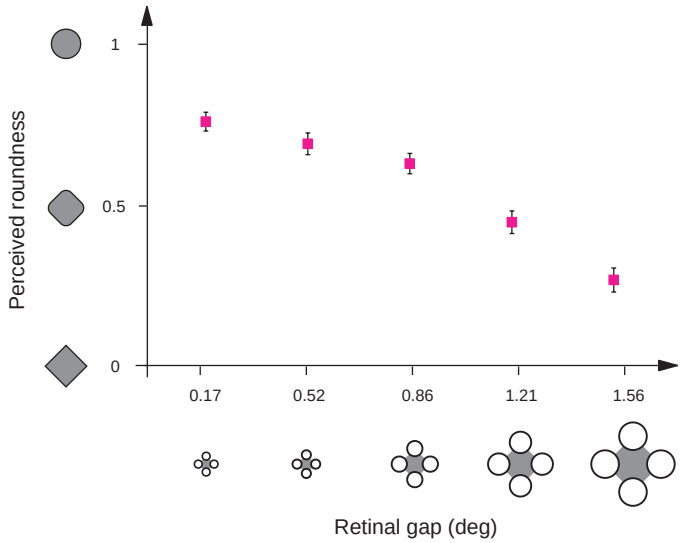

Figure 5. Roundness estimates as a function of retinal gap. Data refer to animated events in which a display with 3.5° retinal gaps shrank and reached each of the minimum values shown in abscissa. Observers estimated the roundness of the maximally contracted occluded shape on a subjective scale between 0 (perfectly rectilinear diamond) and 1 (circle).

Figure 6. The grey region is amodally completed as a truncated square in (b) and as a hexagon in (a). Data obtained in a probe localization task indicate that the interpolated trajectory is closer to good continuation in (b), where T-junction stems are vertical/horizontal, and closer to minimal path in (a), where T-junction stems are oblique and bilateral symmetry along a vertical axis runs against the perception of a truncated diamond.

Orientation. Kanizsa (1971, 1979) noticed that the pattern in Figure 6b is amodally perceived as a partially occluded truncated square, although the grey region is compatible with the perception of a more symmetric hexagon. This demonstration runs against the general claim that perceptual organization (including amodal completion) tends to correspond

to the maximum degree of global regularity, given the circumstances. However, Srebotnjak (1984) and others (Sgorbissa & Gerbino, 1999; Markovic, 1999) provided clear evidence that good continuation overcomes symmetry only when T-junction stems are vertical/horizontal. In Figure 6a where T-junction stems are oblique, most observers perceive a partially occluded hexagon. Gerbino, Sgorbissa, and Fantoni (2000) utilized a probe localization paradigm and estimated the difference between trajectories interpolated in the two cases illustrated. The interpolated trajectory was closer to good continuation in Figure 6b and closer to minimal path in Figure 6a.

Contour polarity. Take two displays that include the same local pattern of T-junctions (Figure 7). Gerbino and Fantoni (2002) showed that the perceived separation between the two occluded vertices is larger when fragments belong to the contours of two convex diamondlike shapes (Figure 7a) than when they belong to the contour of a concave sand-glasslike shape (Figure 7b).

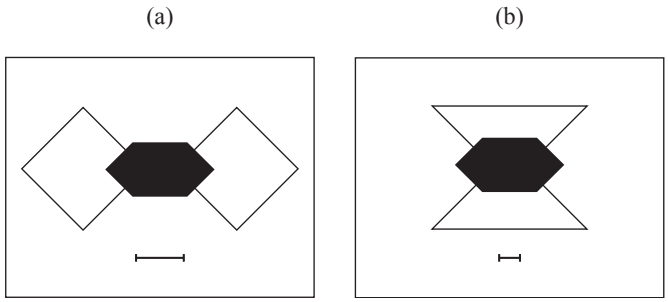

Figure 7. Gerbino and Fantoni (2002) estimated the perceived separation of two occluded vertices, separated by a geometrical distance of 40 pixels. The vertices belonged to two convex shapes (a) and to a concave shape (b). Observers matched it to a horizontal segment of 52 pixels in (a) and 31 pixels in (b).

Global shape. The regularity of the global shape can affect interpolation, as suggested by the following demonstration. Compare two displays containing the same local pattern of T-junctions that are perceived as a partially occluded shape similar to a hexagonlike vertically elongated (Figure 8a) or a squarelike partially occluded shape (Figure 8b). The amodally completed vertex is flatter when global regularity cooperates with minimal path (T-junction stems belonging to the hexagonlike contour, Figure 8a) than when it cooperates with good continuation (T-junction stems belonging to the squarelike contour, Figure 8b).

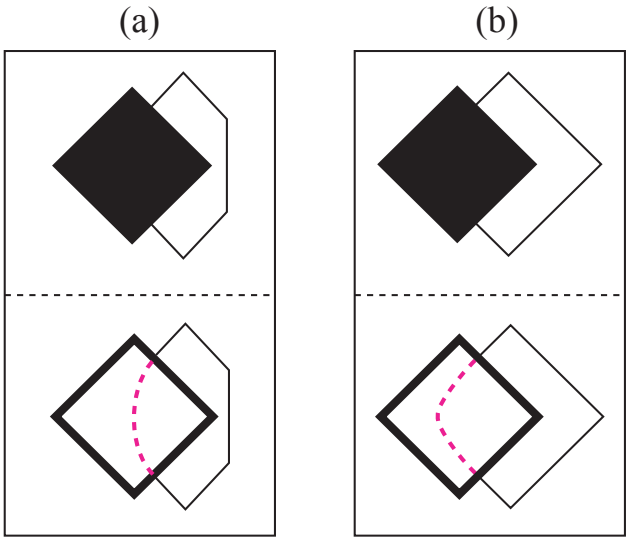

Figure 8. The perceptually interpolated angle penetrates in the occluded space more in b, where the global solution is consistent with good continuation, than in a, where the global solution is consistent with minimal path.

The field model described in the next section shares several features of previous models. However, its architecture, based on the weighting of local factors by global variables, makes it sensitive to scale, orientation, contour polarity, and global shape.

The Field Model

Since its early formulations (Wertheimer, 1923), Gestalt theory recognized that perception depends on several organizing factors and hypothesized integration mechanisms such as algebraic summation and winner-take-all (Metzger, 1954, pp. 135-136). Perceived shapes can be modeled as products of the distribution of context-sensitive forces (Koffka, 1935). Gestalt "laws" proposed for grouping and figure/ground articulation are candidate factors for explaining interpolation.

The present version of our model applies to the interpolation of separate fragments by virtual lines, as well as to prototypical superpositions of flat laminas leading to 90° T-junctions (amodal contours) or 90° L-junctions (modal contours). The effect of nonprototypical T- or L-junctions on interpolation trajectories can be predicted by adding another local parameter. For the sake of simplicity, here we discuss a version of the model that does not include junction amplitude among the relevant parameters.

Interpolation is modeled as the product of three factors: smooth closure (SC), good continuation (GC), and minimal path (MP).

- SC: It is utilized as a superordinate principle that modulates the rivalry between GC and MP, forcing the trajectory to be close and continuous everywhere.

- GC: It is specified by the function that describes the image contour between an endpoint and the first point of inflection, as originally proposed by Wertheimer (1923). Note that such a definition is not local. For instance, the GC interpolation of a partially specified circle is an arc of the same circle and not a sharp vertex made of two intersecting tangents at endpoints.
- MP: It implements the law of proximity at the contour level (or the combination of convexity and minimal area at the surface level).

In the case of partially specified angles (i.e., convergent fragments with intersecting GC extrapolations), GC alone would lead to a sharp vertex (GC-line solution); whereas MP alone would lead to closure by a straight segment with discontinuities at endpoints (MP-line solution).

Elements of the Model

Angles between GC and MP lines are called GC-MP angles. A fragment pair is defined by the following properties:

- curvatures C_1 and C_2;
- endpoints P_1 and P_2, corresponding to edgel positions in the plane;
- edgel orientations α and β, corresponding to the two GC-MP angle sizes.

Each fragment of a pair generates a GC field and a MP field. Every field is characterized by two functions that determine vector orientations and magnitudes at every point of the plane. The model applies to rectilinear and curvilinear fragments integrated by virtual, amodal, and modal trajectories. To simplify the description of the model, all examples in the following figures will refer to amodal completion in occlusion patterns. Figure 9 illustrates GC and MP fields generated by a pair of convergent rectilinear fragments with intersecting GC extrapolations. The GC-orientation function depends on the shape of specified contours. To embody the constancy of curvature of individual extrapolations, the local orientation of the GC vector is defined by the tangent to the curve that describes the relevant image fragment (i.e., the line between the endpoint and the first point of inflection or discontinuity, as proposed in the above definition of GC). When fragments are rectilinear, all GC vectors are parallel (as in Figure 9a). The MP-orientation function depends on the relative position of the two endpoints. Convergent rectilinear fragments with intersecting GC extrapolations (as in Figure 10a) generate two opposite fields in which all MP-vector pairs are parallel to the MP line (as in Figure 9b). Convergent rectilinear fragments with nonintersecting GC extrapolations (as in Figure 11b) generate MP-vector pairs that rotate around the midpoint of the MP-line solution (as in Figure 15).

The GC-magnitude function reaches its maximum at endpoints. The point of decay to zero depends on the fragment-pair type (with/without intersecting extrapolations). The MP-magnitude function grows from zero at fragment endpoints to a maximum at the MP-line midpoint (Figure 9). Note that the minimum of the GC-magnitude function is coincident with the maximum of the MP-magnitude function and vice versa. In accordance with previous results (Takeichi, 1995; Sgorbissa & Gerbino, 1999; Gerbino & Fantoni, 2000; Fantoni & Gerbino, 2001; Fantoni, Sgorbissa, & Gerbino, 2001) and with previous theoretical conceptualizations (Wertheimer, 1923; Metzger, 1954; Kanizsa, 1979), GC- and MP-magnitude functions are context-sensitive monotonic functions (Figure 29).

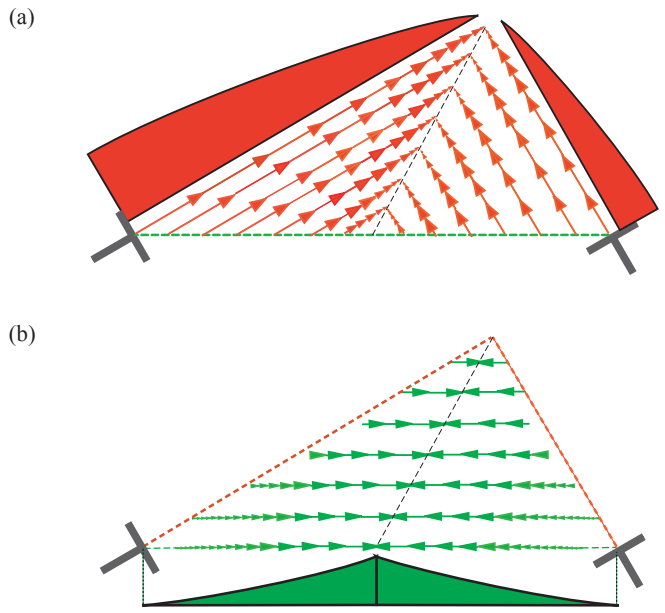

Figure 9. Two convergent rectilinear fragments with intersecting GC extrapolations generate two GC fields and two MP fields. As shown in a, vectors of each GC field are parallel to the corresponding edgel orientation. The magnitude of GC vectors is maximum at endpoints and decays to zero at the median of the triangle bounded by GC and MP lines. As shown in b, all MP vectors are parallel to the MP line. MP-vector magnitudes are null at endpoints and grow to their maximum at the median of the triangle.

The GC-magnitude function is modulated by:

- the absolute quantity of image fragments (GC strength varies as a direct function of the retinal length of image fragments);
- the proportion of specified-to-total contour or support ratio (GC strength varies as a direct function of the support ratio);
- the absolute orientation of image fragments (GC strength varies as an inverse function of the departure from cardinal axes);

- the global shape of the fragmented configuration (for instance, the magnitude of GC vectors is larger if image fragments belong to the contour of a regular shape like a square with missing corners, Figure 8b).
- the convexity/concavity of the interpolated contour (for instance, the magnitude of GC vectors is larger if image fragments belong to the concave contour of a sand-glasslike shape, Figure 7b).

The MP-magnitude function is modulated by:

- the absolute size of the retinal gap between endpoints (MP strength varies as a direct function of endpoint separation);
- the absolute orientation of the two image fragments (MP strength varies as an inverse function of the departure from cardinal axes);
- the global shape of the fragmented configuration (for instance, the magnitude of MP vectors is larger if image fragments belong to the contour of a regular shape like an elongated hexagon with a missing side, Figure 8a).
- the convexity/concavity of the interpolated contour (for instance, the magnitude of MP vectors is larger if image fragments belong to convex contours of the two partially occluded diamonds, Figure 7a).

The trajectory is determined by the bilateral concatenation of GC- and MP-vector sums, starting from each edgel. The two branches of the interpolated trajectory grow out of edgels and smoothly join each other (see Figure 13 for angle completions, and Figure 18 for circular-arc completions).

The only free parameter of the model is GC-MP contrast, the relative difference between the maximum strengths of GC and MP vectors. The internal consistency of the model is evaluated in the following way: GC-MP contrast is set to a particular value to fit empirical data obtained in specific conditions; then, the model is tested by generating predictions consistent with values of GC-MP contrast modulated by figural and viewer-dependent variables and matching them to new empirical data.

Domain of the Model and Properties of Component Fields

Taking into account the local properties of the retinal input and the dynamic structure of the VI process, we can identify a field model applicability domain (FMAD), corresponding to the spatial domain in which closed and smooth interpolating trajectories are generated to connect a fragment pair without uncertainty. A fragment pair belonging to the FMAD is associated to a specific interpolation region (IR) where interpolation trajectories can be generated. In our model, GC and MP fields are null outside the IR.

Rectilinear Fragments

Consider a partially occluded shape with rectilinear sides (Figure 10a). The two GC-MP angles that share the MP line are opposite when the two GC extrapolations intersect (Figure 10b). When one GC extrapolation intersects the other fragment (including the limiting case of parallel fragments with an offset), alternate GC-MP angles are obtained (Figure 10b).

Cases with opposite and alternate GC-MP angles constitute two subdomains of the FMAD for partially specified shapes with rectilinear sides:

(a) rectilinear convergent fragments with intersecting GC extrapolations, as in partially occluded angles (Figure 10), dotted intersecting lines, and the Koffka cross;

(b) rectilinear convergent fragments with nonintersecting GC extrapolations (Figure 11), apart from limiting cases described in the next paragraph (Figure 16).

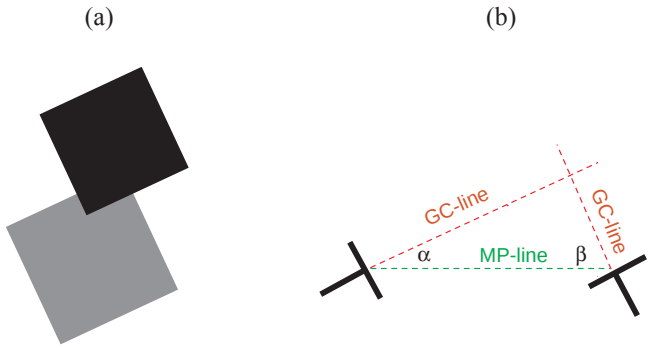

Figure 10. The generic occlusion of a convex vertex in a illustrates the case of convergent rectilinear fragments with intersecting GC extrapolations and opposite GC-MP angles, described in b.

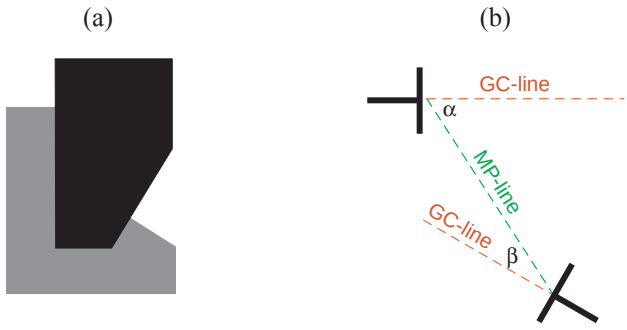

Figure 11. The occlusion of convex and concave adjacent portions in a illustrates the case of convergent rectilinear fragments with nonintersecting GC extrapolations and alternate GC-MP angles.

Opposite GC-MP angles (rectilinear case). All types of angle completions belong to the subdomain defined by opposite GC-MP angles. Their IR is a GC-MP triangle, conveniently conceived as the juxtaposition of two triangles, each defined by the MP line, the relevant

GC lines, and the IR median (Figure 12). The IR median is the line that connects the MP-line midpoint with the GC vertex (i.e., the intersection of GC extrapolations).

The asymmetric occlusion of a rectilinear angle corresponds to the generic case of angle completion, in which the left GC-MP angle α is different from the right GC-MP angle β. The symmetric occlusion of a rectilinear angle corresponds to the specific case in which $\alpha=\beta$.

GC-magnitude functions have a maximum at endpoints and decay to zero at the intersection of the two GC lines. The maxima of GC-magnitude functions are proportional to the GC sides of the IR. Therefore, GC-magnitude maxima differ when the IR is asymmetric (Figure 9a). Independent of IR symmetry, MP-magnitude functions grow from 0 at endpoints to a maximum at the MP-line midpoint. Left and right MP functions (one for each portion of the IR, Figure 9b) are always identical.

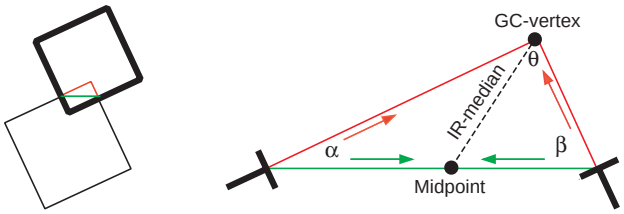

Figure 12. The IR in the generic case of angle completion illustrated in Figure 10. The relevant portion of amodal space is the GC-MP triangle bounded by the two GC extrapolations meeting at the GC vertex and by the MP line. The interpolation angle defined by the two GC extrapolations is θ. As in Figure 10b, α and β are the angles between GC extrapolations and the MP line. Keeping θ constant, the difference between α and β determines the amount of occlusion asymmetry in each specific case.

Consider GC and MP vectors in the left and right IR portions. As regards vector orientations, all GC vectors are parallel to the relevant GC line (either left or right) and point away from the endpoints, whereas all MP vectors are parallel to the MP line and point toward its midpoint. As regards magnitudes, the reference line for both GC and MP vectors is the IR median. All GC vectors along a parallel to the IR median are equal to the length of the GC vector at the intersection between the parallel to the IR median and the relevant GC line. Such a length depends on the GC-magnitude function (see Equation 11. All MP vectors along a parallel to the IR median are equal to the length of the MP vector at the intersection between the parallel to the IR median and the MP line. Such a length depends on the MP-magnitude function (see Equation 12).

Starting from each endpoint, the model computes the sum of GC and MP vectors at successive locations and generates a monotonic interpolation trajectory with a maximum at the cross-point with the IR median. The tangent at such a maximum is parallel to the MP line (Figure 13). As GC-MP contrast increases, the interpolation trajectory approximates the GC-line solution.

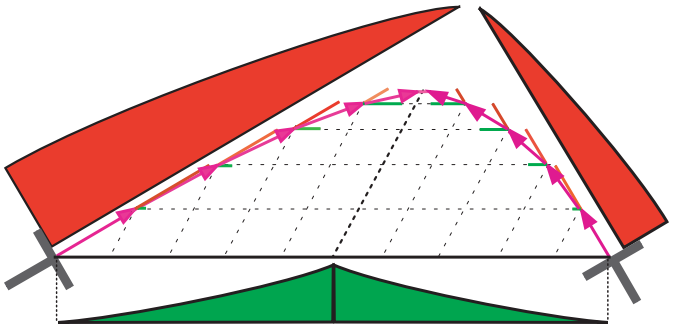

Figure 13. A step-by step trajectory generated by the vector sum procedure in the generic case of angle completion. Starting from each endpoint, the chaining of GC- and MP-vector sums at successive locations generates an ordinate set of local tangents to a monotonic interpolation trajectory with a maximum at the cross-point with the IR median.

Alternate GC-MP angles (rectilinear case). Contrary to opposite GC-MP angles with intersecting GC extrapolations, alternate GC-MP angles define two open regions, one for each of the half-planes defined by the MP line. According to constraints described in the next section, patterns with alternate GC-MP angles include fragment pairs with an offset.

To determine a closed IR, we assume that its final shape is a GC-MP bow tie (Figure 14) composed by two triangles with vertical angles at the MP-line midpoint (i.e., the knot of the tie). Like the GC-MP triangle, the GC-MP bow tie is composed by two triangles bounded by the MP line, the two relevant GC lines, and a central IR line.

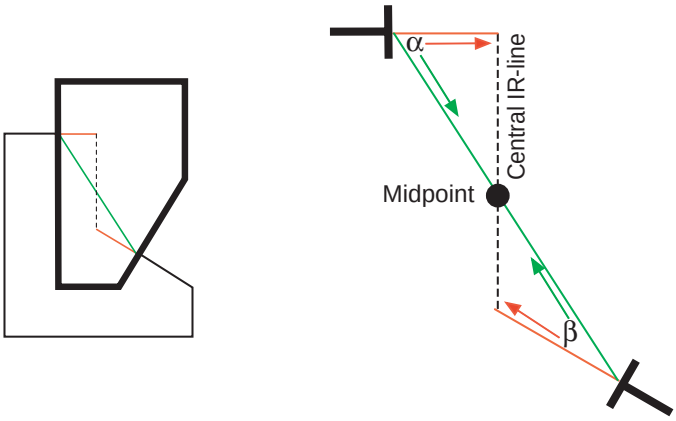

Figure 14. The IR for the generic case of convergent rectilinear fragments with nonintersecting GC extrapolations (see Figure 11). The reference fragment bounding the larger GC-MP angle is horizontal. The central IR line is the normal to the reference fragment through the MP-line midpoint. All interpolation trajectories generated by our field model are included in the GC-MP bow tie bounded by the two GC lines, the MP line, and the central IR line.

The bow tie is obtained in the following way. First, the fragment with the larger GC-MP angle is chosen as a reference. Then the normal to the GC extrapolation of the reference fragment through the MP-line midpoint is defined as the central IR line, analogous to the IR median. Given two candidate GC normals, the rationale for selecting the normal to the extrapolation of the reference fragment is the minimization of the global perimeter of the bow tie. Such a normal is the shorter of the two and minimizes the relevant GC lines.

Patterns with alternate GC-MP angles include generic cases with $\alpha \neq \beta$ and specific cases with $\alpha = \beta$ (i.e., parallel fragments with an offset). Generic and specific cases are solved using the procedure valid in the opposite GC-MP angle subdomain.

Each GC-magnitude function has a maximum at the endpoint and decays to zero at the corresponding intersection of the GC line with the central IR line. All MP vectors point toward the MP-line midpoint. Starting from each endpoint, the model computes the sum of GC and MP vectors at successive locations and generates an interpolation trajectory with an inflection at the MP-line midpoint. Tangents in the neighborhood of the inflection are nearly parallel to the central IR line (Figure 15). As GC-MP contrast increases, the interpolation trajectory approximates the composite path with abrupt changes of curvature defined by the two GC lines and the central IR line.

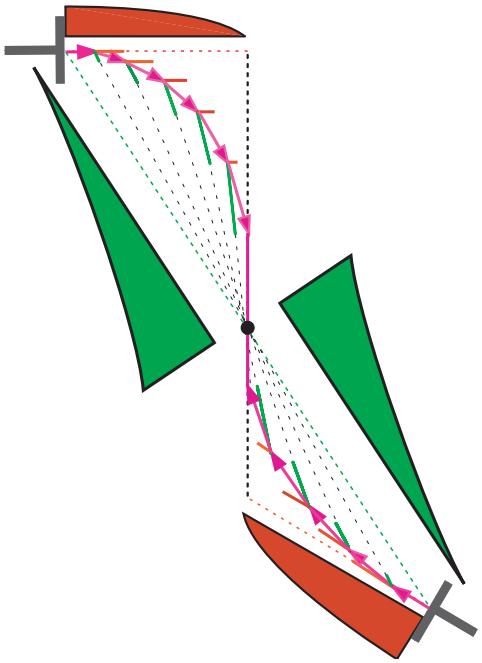

Figure 15. A step-by-step trajectory generated by the vector sum procedure in the generic case of convergent rectilinear fragments with nonintersecting GC extrapolations (see Figure 11 and Figure 14). Starting from each endpoint, the chaining of GC- and MP-vector sums at successive locations generates an ordinate set of local tangents to an interpolation trajectory with an inflection at the MP-line midpoint.

A compatibility criterion for rectilinear fragments. Compatibility criteria are inferred from properties of our field model. A basic compatibility criterion for the interpolation of rectilinear fragments is the following: the sum of the two GC-MP angles must be less than 180°. When $\alpha + \beta \geq 180°$, no trajectory can be found because of the structural indeterminacy of the decay points of GC-magnitude functions. There are two limiting cases, one for each subdomain of the FMAD for rectilinear fragments (Figure 16).

- *Limiting case for opposite GC-MP angles.* It occurs if one GC-MP angle is null. Both angles can be null but only one cannot: if $\alpha \neq \beta$, then $\alpha > 0$ and $\beta > 0$. Gerbino's illusion (Figure 16a) demonstrates that partially occluded polygons with one null GC-MP angle are visually intriguing (Gerbino, 1978; Da Pos & Zambianchi, 1996).
- *Limiting case for alternate GC-MP angles.* It occurs if one GC-MP angle is larger than 90°. If $\alpha \neq \beta$, then $\alpha < 90°$ and $\beta < 90°$. Amodal completion of polygons with one GC-MP angle larger than 90° is phenomenally undefined (Figure 16b).

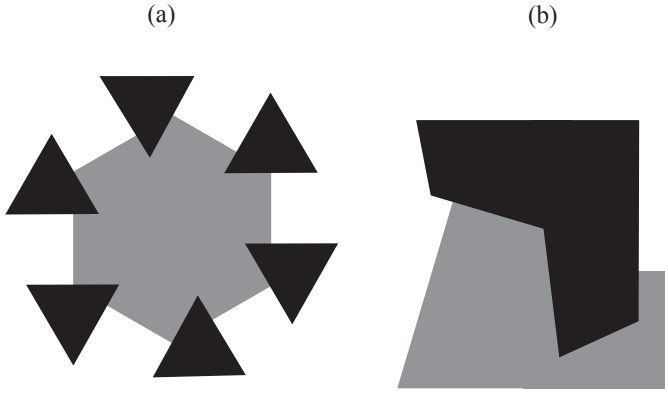

Figure 16. Limiting cases of the FMAD for rectilinear fragments. In a (opposite GC-MP angles), a distorted hexagon is perceived (Gerbino, 1978). In b (alternate GC-MP angles), the partially occluded shape is perceptually undefined.

Curvilinear Fragments

In accordance with the theory of curvature-constraint line (Takeichi et al., 1995), our model interpolates curvilinear fragments by means of trajectories with a maximum of three inflections.

Also the FMAD for curvilinear fragments can be articulated into two subdomains, one for opposite and one for alternate GC-MP angles. Both subdomains are complex and depend on the shapes and relative positions of arcs to be interpolated. Let us analyze them with reference to some prototypical cases with circular-shaped fragments.

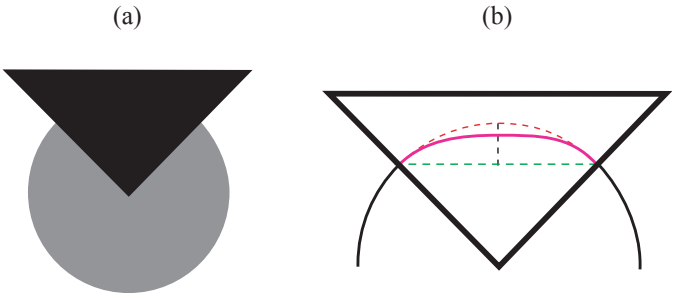

Figure 17. Our field model predicts the perceived flattening of the partially occluded circle in a. The predicted trajectory that interpolates two co-circular fragments (continuous line in b) is a flattened arc included between the pure GC solution and the MP line.

Opposite GC-MP angles (curvilinear case). The occlusion of a circle illustrates the case of opposite GC-MP angles generated by co-circular arcs (Figure 17). The corresponding IR is identified by the same procedure utilized for rectilinear fragments with opposite GC-MP angles. It is the region included between the rectilinear MP line (green dotted line in Figure 17b) and the curvilinear GC extrapolations (red dotted line in Figure 17b). By analogy with the rectilinear case, the central IR line connects the junction of the two symmetric GC extrapolations with the MP-line midpoint.

Contrary to predictions from circular-arc models (Ullman, 1976; Kellman & Shipley, 1991) and spline models, our field model generates a flattened arc, as a function of GC-MP contrast (Figure 18). The flattening observed in static configurations is consistent with a dynamic effect we observed using a special kind of apparent rest display (Metelli, 1940).

When an asymmetric 3-sector fan rotates on top of a partially occluded concentric disk, the disk looks nonrigid (Movie 1) and the amodal contour is perceptually flattened. The lack of rigidity depends on the tendency of shapes to keep a stable orientation (Musatti, 1924, 1975) and to the flattening of amodally interpolated contours.

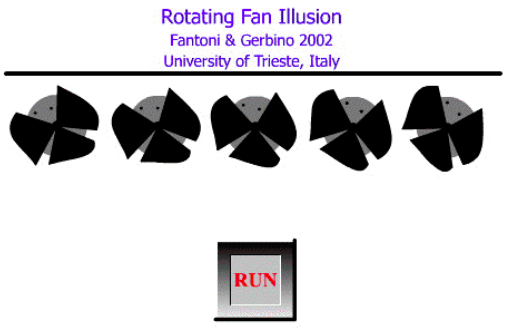

Movie 1. Demonstration of the rotating fan illusion.

All co-circular arcs are compatible. Non-co-circular arcs with opposite GC-MP angles and intersecting GC extrapolations are also compatible. In such a case, the IR is bounded by the MP line and by two curved GC extrapolations whose intersection can be either continuous or discontinuous. Just as in the rectilinear case, the interpolated trajectory is always included in the asymmetric ($\alpha \neq \beta$) convex hull bounded by the two GC extrapolations, and the MP line and its tangent at the point of intersection with the IR median is parallel to the MP line.

Non-co-circular arcs with opposite GC-MP angles but nonintersecting GC extrapolations are not compatible with the field model.

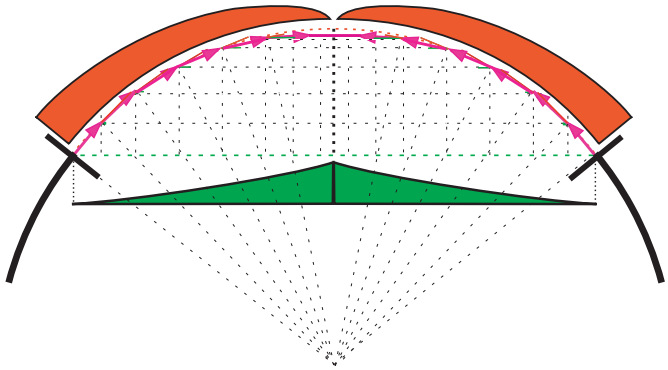

Figure 18. A step-by-step interpolation generated by the constrained extrapolation of co-circular arcs, according to the vector sum procedure. Starting from each endpoint, the chaining of sums of GC vectors (red) and MP vectors (green) at successive locations generates an ordinate set of local tangents to the interpolation trajectory (pink). Such a solution is flatter than the circular arc solution (red dotted line) and has a maximum at the cross-point with the IR median (black dotted line). GC vector magnitude functions refer to a curved abscissa, consistent with the assumption that each GC extrapolation preserves the global curvature of the corresponding image fragment.

Alternate GC-MP angles (curvilinear case). Patterns with alternate GC-MP angles can be obtained by either homogeneous or heterogeneous non-co-circular arcs. Two non-co-circular arcs are homogeneous if their concavities are on the same side. This is an intentionally loose definition that can be clarified only by the following examples.

A typical pattern with alternate GC-MP angles and homogeneous non-co-circular arcs is shown in Figure 19a. Such arcs belong to different circles, one eccentrically included within the other. The corresponding IR is identified by the same procedure utilized for rectilinear fragments with alternate GC-MP angles (Figure 19b). The interpolation of homogeneous non-co-circular arcs generates a trajectory with two points of inflections, supporting the perception of a partially occluded snail-like shape.

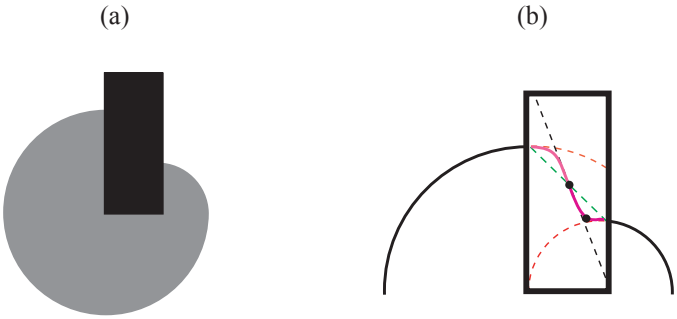

Figure 19. The partially occluded snaillike shape perceived in a illustrates the interpolation of two homogeneous non-co-circular arcs. The field model predicts that the two arcs are interpolated by the continuous trajectory in b, characterized by two inflections (black dots on the pink trajectory).

Heterogeneous non-co-circular arcs always define a pair of alternate GC-MP angles. Figure 20 and Figure 21 illustrate two typical cases, in which the corresponding IRs can be identified by the same procedure used for rectilinear fragments with alternate GC-MP angles. Instead of using parameters proposed by Takeichi et al. (1995, pp. 381-382), we distinguish the following two cases of alternate GC-MP angles:

- internal alternate GC-MP angles, located inside the convex regions bounded by the GC extrapolations, the central IR line and the MP line, in which our model generates a trajectory with one inflection (Figure 20b);
- external alternate GC-MP angles, located outside the convex regions bounded by the GC extrapolations the central IR line and the MP line, in which our model generates a trajectory with three inflections (Figure 21b).

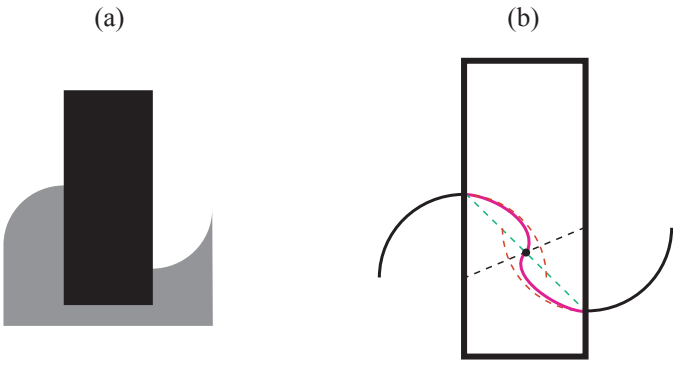

Figure 20. The wave pattern in a derives from the interpolation of heterogeneous arcs with internal alternate GC-MP angles. The interpolated trajectory in b has one inflection and represents a compromise between GC extrapolations and the MP line.

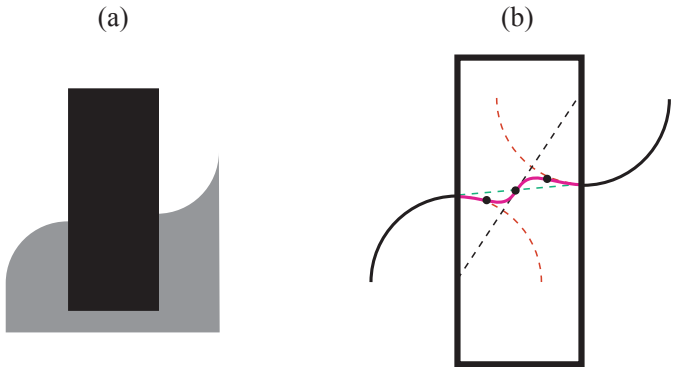

Figure 21. In a, the arcs define a pattern of external alternate GC-MP angles. As shown in b, the field model generates a trajectory with three inflections, which represents a complex compromise between GC extrapolations and the MP line.

A compatibility criterion for circular fragments. Arcs with opposite GC-MP angles and intersecting GC extrapolations are always compatible. Other non-co-circular arcs are compatible if a closed bow tie IR can be defined. This is the case if the following compatibility criterion is satisfied:

- one straight line through the MP-line midpoint must be normal to the GC extrapolation that bounds the larger GC-MP angle and must intersect the other.

Dynamic Compatibility Criteria

Dynamic compatibility criteria are more general than geometric compatibility criteria. They allow for the interpolation of various types of fragments incompatible with relatability constraints: for instance, rectilinear fragments with opposite GC-MP angles whose sum is higher than 90° and lower than 180°; rectilinear fragments with alternate GC-MP angles; circular fragments with intersecting GC extrapolations and opposite GC-MP angles whose sum is higher than 90°; and circular fragments with alternate GC-MP angles.

Dynamic compatibility criteria are a consequence of the tendency to minimize inflections of interpolated contours embodied in our field model and explicitly considered by the curvature-constraint-line theory. However, they are more precise than the curvature-constraint-line theory and other geometric approaches (including relatability), given that one criterion and two limiting cases are specific to rectilinear fragments.

To measure the degree of compatibility of two fragments, we suggest the following candidate parameters: stability of model's output; number of inflections of the generated trajectory; and, total amount of bending energy (Equation 2). The validity of such parameters should be tested psychophysically.

An Algorithm for Angle Completion

In the "Introduction," we mentioned several reasons for studying the completion of partially specified angles. Here we provide formal definitions appropriate for the interpolation of partially specified rectilinear angles, including cases of symmetric (Figure 1a) and asymmetric (Figure 10a) occlusion. Readers who are not interested in the details of the algorithm can skip this section and jump to "Properties of Trajectories for Angle Interpolation."

The portion of 2D space included within GC and MP lines is the GC-MP triangle. Given two T-junctions (T_{Lx} and T_{Rx}) and a set of contextual conditions, the model generates GC and MP fields that fill the IR (Figure 9). For each GC-MP contrast value, the chaining of GC- and MP-vector sums determines a unique trajectory. The interpolation trajectory is characterized by a penetration value corresponding to the relative location of the cross-point along the IR median. The penetration value identifies the maximum of the trajectory.

Figure 22 provides the definitions used in subsequent demonstrations. To obtain a convenient Cartesian representation of the GC-MP triangle, the middle point of the MP line is located at the origin O= (0, 0). The MP line connecting the left terminator T_{Lx} and the right terminator T_{Rx} is made to coincide with the x-axis. The median of the GC-MP triangle is {M}, the line that connects O with the GC vertex V. The left and right sides of the GC-MP triangle (corresponding to $T_{Lx}V$ and $T_{Rx}V$ lines) are A_L and A_R. For T_{Lx} and T_{Rx} stems, respectively, we define the two versors (oriented segments of unitary length): $\hat{\mathbf{I}}_{Lx} = (\cos\alpha, \sin\alpha)$ and $\hat{\mathbf{I}}_{Rx} = (-\cos\beta, \sin\beta)$.

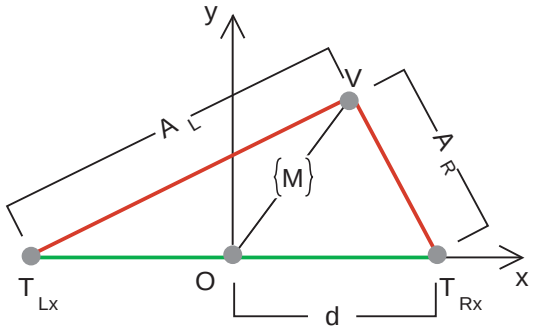

Figure 22. Cartesian representation of the GC-MP triangle for a generic case of vertex occlusion.

Taking d as the half base of the GC-MP triangle, the coordinates of its vertices are:

$$T_{Lx}= (-d, 0);\ T_{Rx}= (d, 0);$$

$$V= (d \sin(\beta-\alpha)/\sin(\beta+\alpha),\ 2\, d \sin(\alpha) \sin(\beta)/\sin(\beta+\alpha))$$

The lengths of the relevant GC extrapolations are:

$$A_L= 2\, d \sin(\beta)/\sin(\beta+\alpha);$$

$$A_R= 2\, d \sin(\alpha)/\sin(\beta+\alpha)\ .$$

The (x, y) points of the IR median {M} through V and O satisfy the following equation:

$$y = \frac{2\sin(\alpha)\sin(\beta)}{\sin(\beta-\alpha)}x \qquad (6)$$

The GC vectors $\mathbf{V}_{GC}(\mathbf{r})$ are directed along $\hat{\mathbf{I}}_{Lx}$ in the left portion of the GC-MP triangle (called $\mathbf{R}_L$), relative to {M}, and along $\hat{\mathbf{I}}_{Rx}$ in the right portion (called $\mathbf{R}_R$). The MP vectors $\mathbf{V}_{MP}(\mathbf{r})$ are directed along the versor of the x-axis $\hat{\mathbf{A}}_{Lx}= (1, 0)$ in $\mathbf{R}_L$ and in the opposite direction, $\hat{\mathbf{A}}_{Rx}= (-1, 0)$, in $\mathbf{R}_R$.

Therefore the generic GC vector and the generic MP vector are represented by:

$$\mathbf{V}_{GC}(\mathbf{r}) = V_{GC}(\mathbf{r})\hat{\mathbf{I}}_{Lx};\ \mathbf{V}_{MP}(\mathbf{r}) = V_{MP}(\mathbf{r})\hat{\mathbf{A}}_{Lx}$$

$$\text{for } x < y\ (\sin(\beta-\alpha)/2\sin(\alpha)\sin(\beta)) \text{ and } \mathbf{r} \in \mathbf{R}_L$$

$$\mathbf{V}_{GC}(\mathbf{r}) = V_{GC}(\mathbf{r})\hat{\mathbf{I}}_{Rx};\ \mathbf{V}_{MP}(\mathbf{r}) = V_{MP}(\mathbf{r})\hat{\mathbf{A}}_{Rx}$$

$$\text{for } x > y\ (\sin(\beta-\alpha)/2\sin(\alpha)\sin(\beta)) \text{ and } (\mathbf{r} \in \mathbf{R}_R)$$

where $V_{GC}(\mathbf{r})$ and $V_{MP}(\mathbf{r})$ indicate, respectively, GC- and MP-vector lengths at the point $\mathbf{r}$ of the plane $\mathbf{R}$.

To implement smooth closure, GC- and MP-vector magnitudes are such that at T-junctions $V_{GC}(\mathbf{r})= V_{GC\_max}$ and $V_{MP}(\mathbf{r})= 0$, and on the median $V_{GC}(\mathbf{r})= 0$ and $V_{MP}(\mathbf{r}) = V_{MP\_max}$.

As regards vector magnitude functions, given a point in the left portion of the field $\mathbf{r}= (x_0, y_0) \in \mathbf{R}_L$, the GC-vector magnitude depends on the $T_{Lx}P$ length, where P is the intersection between the GC line and the parallel to the median through $\mathbf{r}$ (Figure 23). The $T_{Lx}P$ length is defined by:

$$z_L(x_0, y_0) = \frac{2(d + x_0)\sin(\beta)}{\sin(\beta+\alpha)} - \frac{y_0 \sin(\beta-\alpha)}{\sin(\alpha)\sin(\beta+\alpha)} \qquad (7)$$

The MP-vector magnitude at $\mathbf{r}$ depends on the $T_{Lx}Q$ length, where Q is the intercept of the parallel to the median with the x-axis. $T_{Lx}Q$ is defined by:

$$k_L(x_0, y_0) = d + x_0 - \frac{y_0 \sin(\beta-\alpha)}{2\sin(\alpha)\sin(\beta)} \qquad (8)$$

Analogously, given a point in the right portion of the field, $\mathbf{r} = (x_0, y_0) \in \mathbf{R}_R$, GC- and MP-vector magnitudes depend on $T_{Rx}P$ and $T_{Rx}Q$ lengths, defined, respectively, by:

$$z_R(x_0, y_0) = \frac{2(d - x_0)\sin(\alpha)}{\sin(\beta+\alpha)} + \frac{y_0 \sin(\beta-\alpha)}{\sin(\beta)\sin(\beta+\alpha)} \qquad (9)$$

$$k_R(x_0, y_0) = d - x_0 + \frac{y_0 \sin(\beta-\alpha)}{2\sin(\alpha)\sin(\beta)} \qquad (10)$$

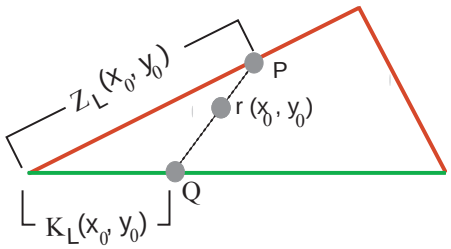

Figure 23. Given a point $r = (x_0, y_0) \in R_L$ on the left of {M}, the GC vector magnitude depends on the point $Z_L(x_0,y_0)$, where the parallel to {M} intersects the left GC line. The MP-vector magnitude depends on the point $K_L(x_0,y_0)$, where the parallel to {M} intersects the left half of the MP line.

$V_{GC}(\mathbf{r})$ is a function of z, whereas $V_{MP}(\mathbf{r})$ is a function of k. Assuming that each function is a quadratic (because of its formal simplicity) $V_{GC}(\mathbf{z})$ and $V_{MP}(\mathbf{k})$ take the following form (Figure 24):

$$V_{GC}(\mathbf{z}) = V_{GC\_\max}\left[1 - \left(\frac{z}{A}\right)^2\right] \quad (11)$$

$$V_{MP}(\mathbf{k}) = V_{MP\_\max}\left(\frac{k}{d}\right)^2 \quad (12)$$

where A corresponds to the length of the relevant GC line (left or right).

One can see that $V_{GC}(\{M\})= 0$; $V_{MP}(T_{Lx})= V_{MP}(T_{Rx})= 0$; $V_{MP}(\{M\}) = V_{MP\_max}$. In symmetric cases, $V_{GC}(T_{Lx})= V_{GC}(T_{Rx})= V_{GC\_max}$; in asymmetric cases, $V_{GC}(T_{Lx})$ and $V_{GC}(T_{Rx})$ are proportionally increased or decreased, relative to V_{GC_max}, as a function of the difference between the two GC-MP angles.

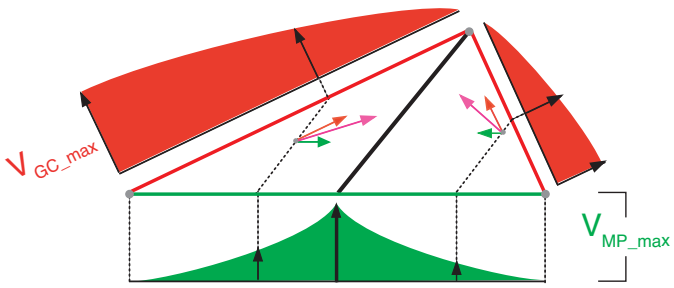

Figure 24. GC- and MP-vector magnitudes depend on the GC-decay function and the MP-growth function. Left and right GC magnitudes have their maxima at T-junctions. One GC-magnitude function is a compressed analogue of the other. The degree of compression is proportional to the difference between the two GC-MP angles. Left and right MP-vector magnitudes grow from 0 at T-junctions to the maximum V_{MP_max} at {M}. Independent of the symmetry of the GC-MP triangle, MP-magnitude functions are always identical.

Given such quadratic functions for $V_{GC}(\mathbf{z})$ and $V_{MP}(\mathbf{k})$, the only free parameter of the model is the GC-MP contrast. The definition of GC-MP contrast given in (Equation 1) can be rewritten as:

$$GC\text{-}MP\ contrast = \frac{V_{GC\_\max} - V_{MP\_\max}}{V_{GC\_\max} + V_{MP\_\max}} \quad (13)$$

The GC-MP contrast value varies between –1, when V_{GC_max} is null (minimum IT penetration) and 1, when V_{MP_max}, is null (maximum IT penetration). The amount of penetration increases as GC-MP contrast increases (Figure 25).

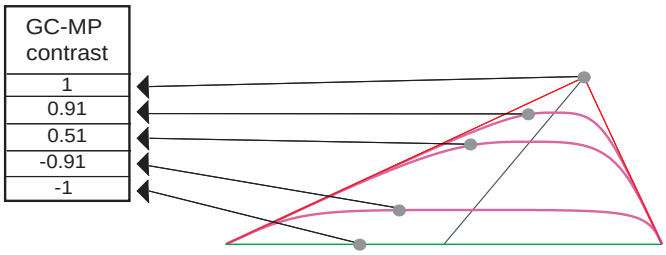

Figure 25. The GC-MP contrast modulates the amount of penetration of the trajectory generated by our field model. As GC-MP contrast approaches 1, the interpolated trajectory approximates the GC solution.

Obviously, one can choose other functions for $V_{GC}(\mathbf{z})$ and $V_{MP}(\mathbf{k})$. However, as it will become clear in the following, left and right trajectories join by preserving continuity if two fundamental conditions, both derived from the smooth closure, are satisfied:

$V_{GC}(T)= V_{GC\_max}$ *and* $V_{GC}(\{M\})= 0$;

$V_{MP}(T)= 0$ *and* $V_{MP}(\{M\})= V_{MP\_max}$

Our model generates a smooth interpolating curve under the requirement that the resulting sum vector $\mathbf{V}_{RS}(\mathbf{r})= \mathbf{V}_{GC}(\mathbf{r}) + \mathbf{V}_{MP}(\mathbf{r})$ is tangent to the curve in every point. For any given point (x_0, y_0) of the interpolation trajectory, the Cartesian components of the resulting vector $\mathbf{V}_{RS}(\mathbf{r})= (RS_x, RS_y)$ are:

$$RSx\ (x_0, y_0) = V_{GC}(\mathbf{z})\cos(\alpha) + V_{MP}(\mathbf{k}) \quad \text{for } \mathbf{r} \in \mathbf{R}_L \quad (14)$$

$$RS_y\ (x_0, y_0) = V_{GC}(\mathbf{z})\sin(\alpha)$$

$$RS_x\ (x_0, y_0) = -V_{GC}(\mathbf{z})\cos(\alpha) - V_{MP}(\mathbf{k}) \quad \text{for } \mathbf{r} \in \mathbf{R}_R \quad (15)$$

$$RS_y\ (x_0, y_0) = V_{GC}(\mathbf{z})\sin(\alpha)$$

The model requires that the first derivative of the interpolating curve, in the left and right portions of the GC-MP triangle, is given by the tangent of the slope of $\mathbf{V}_{RS}(\mathbf{r})$:

$$y' = \frac{RS_y(x,y)}{RS_x(x,y)} \quad (16)$$

Obviously, the interpolated path and its first derivative are continuous. Notice that in T_{Lx} and T_{Rx} the following holds: $y'(T_{Lx})= \tan(\alpha)$ and $y'(T_{Rx})= -\tan(\beta)$, respectively;

whereas y'({M})= 0, for both solutions on left and right sides.

Properties of Trajectories for Angle Interpolation

In symmetric occlusion, where $\alpha = \beta$, the geometry of the model is simplified. As a consequence of the mirror symmetry of left and right vector fields, the generated trajectories are symmetric with respect to the GC-MP triangle median, which lies on the y-axis. The V_x coordinate becomes 0. Equations z_L (Equation 7) and z_R (Equation 9) as well as k_L (Equation 8) and k_R (Equation 10) become equal. Therefore, the symmetric left and right trajectories meet on the y-axis at the cross-point with the GC-MP triangle median. Such a property holds also in asymmetric occlusion, where $\alpha \neq \beta$.

The location of the IT maximum on the GC-MP triangle median is an important general property of field-model trajectories, consistent with empirical data obtained by Fantoni and Gerbino (2001), who used a multiple probe procedure to study amodally perceived trajectories in the symmetric occlusion case ($\alpha = \beta = 45°$) and in two asymmetric occlusion cases ($\alpha = 35°$, $\beta = 55°$; $\alpha = 25°$, $\beta = 65°$). In each case, observers adjusted three differently oriented probes tangent to the amodal trajectory. The orientations of the three probes (relative to the MP line) were as follows: 0° (i.e., parallel to the MP line), $-\alpha/2$ (i.e., the bisector of the α angle); $\beta/2$ (i.e., the bisector of the β angle). Two conditions of retinal size were studied. We used long thin lines as probes to prevent a risk that is present with short probes (or dots). If a short probe were treated as a fragment belonging to the same contour defined by T-junction stems, the interpolated trajectory would be perturbed. Predictions of various models were evaluated by comparing the average intersections of tangent probes with the GC-MP triangle median. Independent of symmetry, probes intersected the median in the following order of closeness to MP: first, the MP-parallel probe; second, the $-\alpha/2$ probe; third, the $\beta/2$ probe. Figure 26 illustrates that such an ordering is predicted by our field model but not by the circular-arc model and by the Hermite spline, which, for small asymmetry, is a good approximation of elastica (as suggested by Sharon et al., 1997).

Fantoni and Gerbino (2001, slide 18) compared the distribution of 18 average localizations of tangent probes (3 probe orientations x 3 occlusion cases x 2 retinal gaps) to predictions of the field model, the circular-arc model and the Hermite spline. Other models that generate approximations to elastica curves do not make obvious predictions and were not considered. A small percentage of variance was explained by the Hermite spline (3%) and the circular-arc model (9%). Instead, more than 75% of the variance was explained by our field model, depending on the specific value of GC-MP contrast (see slide 17 to evaluate the model's robustness). To be fair with competing models, we set GC-MP contrast to different values: 0.95 for the comparison with the Hermite spline and 0.45 for the comparison with the circular arc. The corresponding percentages of variance explained by our field model were 85% and 76%, respectively.

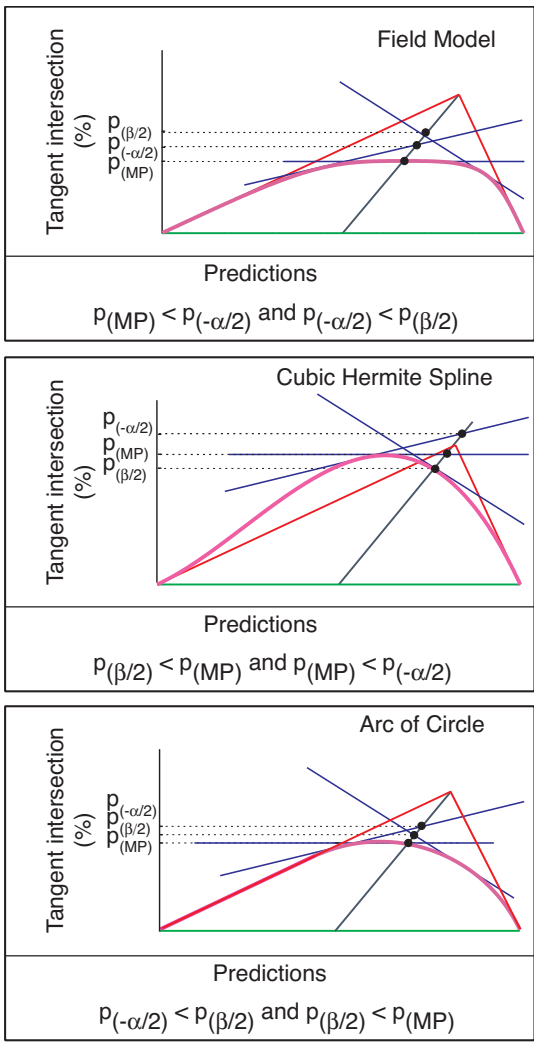

Figure 26. Different models make different predictions about the relative locations of the three tangents. Given a GC-MP triangle with $\alpha < \beta$ and three tangents with slopes 0°, $-\alpha/2$, and $\beta/2$ (relative to the MP line), our field model makes the following ordinal predictions: $P_{(MP)}$ (the intersection between the MP-parallel probe and the GC-MP triangle median) is lower than $P_{(-\alpha/2)}$, which in turn is lower than $P_{(\beta/2)}$. Different orderings are predicted by circular-arc models and the cubic Hermite spline. For the IR shown in this figure ($\alpha = 25°$), Fantoni and Gerbino (2001, slide 16) found that the three intersections for 0°, $-\alpha/2$, $\beta/2$ probes were 86, 90, and 96% with a 3° retinal gap, and 68, 77, and 83% with a 1.5° retinal gap. Tangent intersection values were percentages of the GC-MP triangle median.

Like circular-arc models, the Bézier spline, and possibly some elastica-based models (but differently from the Hermite spline), the field model predicts that in all

occlusion cases the whole family of interpolated trajectories corresponding to different GC-MP contrast values lies inside the GC-MP triangle. It is easy to demonstrate that when $(\alpha - \beta)$ is large, the Hermite spline goes outside the GC-MP triangle.

Another important property of our model is that the penetration of the trajectory decreases as the sum of the two GC-MP angles increases (Figure 27). This is consistent with a quantitative formalization of relatability and with empirical data by Gerbino and Fantoni (2000). We found that the amount of penetration into the GC-MP triangle, estimated by the probe localization procedure, increases as the interpolation angle θ increases. Such a feature is shared by circular-arc models but not by spline models that maintain a constant penetration across different sizes of the interpolation angle.

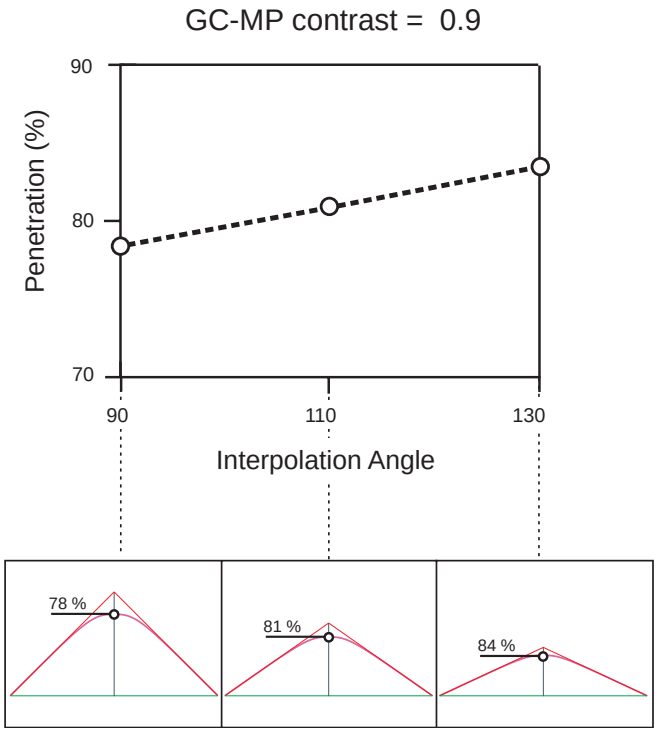

Figure 27. Our field model predicts that the amount of penetration into the GC-MP triangle increases as the size of the interpolation angle increases. The penetration value is a percentage corresponding to the position of the cross-point along the median from the MP-line midpoint to the GC vertex.

Our algorithm generalizes from symmetric to asymmetric occlusion cases by approximating a shearing transformation, very common in nature (Thompson D'Arcy, 1917/1942). The simple shear of a given symmetric trajectory determines a whole set of asymmetric trajectories referred to x_{new}, y_{new} coordinates obtained by tilting the y-axis of original rectangular coordinates by a variable angle w (Figure 28). The algorithm does not implement a perfect simple shear, although the approximation is high at small asymmetries. In the present version of the algorithm, an increasing asymmetry produces an increase of the GC-MP contrast value, which makes the interpolated angle sharper. This feature is desirable given that extreme asymmetric cases correspond to the reduction of the IR and to short distances between a fragment endpoint and the GC vertex.

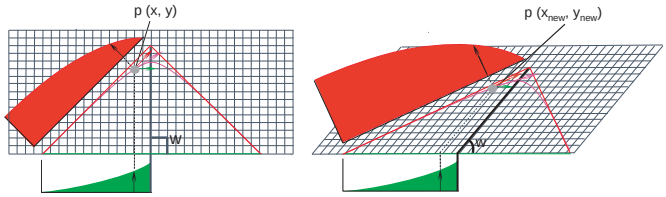

Figure 28. The asymmetric trajectory on the right approximates the simple shear of the symmetric trajectory on the left.

Context Sensitivity of the Interpolated Trajectory

Our field model of VI includes structural and metrical aspects. Under constant structural constraints, the relative strength of GC and MP vectors depends on metrical information. Every resultant that locally defines the interpolated trajectory depends on the strengths of the two component vectors at the relevant location of the GC-MP triangle. This is an original aspect of the model, which generates a VI trajectory by combining two independent factors whose relative strength is affected by contextual variations, depending on the configuration and on viewing conditions. Figure 29 illustrates how different contextual variables interact and determine V_{GC_max} and V_{MP_max}.

At least two viewer-dependent variables (retinal gap and orientation) and one viewer-independent variable are known to affect the interpolation of angles.

(a) *Retinal gap between T-junctions.* We found that the amodal trajectory becomes flatter as the retinal gap between the two T-junctions decreases, keeping other conditions constant. When retinal size was small, observers placed probes closer to the MP line (Gerbino & Fantoni, 2000; Fantoni & Gerbino, 2001, slide 16). According to our field model, as the retinal gap decreases, the MP strength increases faster than the corresponding decrease of the GC vector, that is simply scaled with size. This implies that the penetration of the interpolated trajectory decreases as the observer distance increases (Figure 30). The retinal-gap effect on VI is consistent with data on the salience of illusory contours by Dumais and Bradley (1976).

(b) *Orientation.* Sgorbissa and Gerbino (1999) demonstrated that orientation affects the shape of VI. The orientation effect can be attributed to the combination of direct and mediated effects, which increase the penetration of the interpolated

trajectory when T-junction stems are oriented along cardinal axes (Gerbino, Sgorbissa, & Fantoni, 2000; Fantoni et al., 2001). The direct effect depends on the strengthening of GC along such axes. The mediated effect depends on orientation and form interactions.

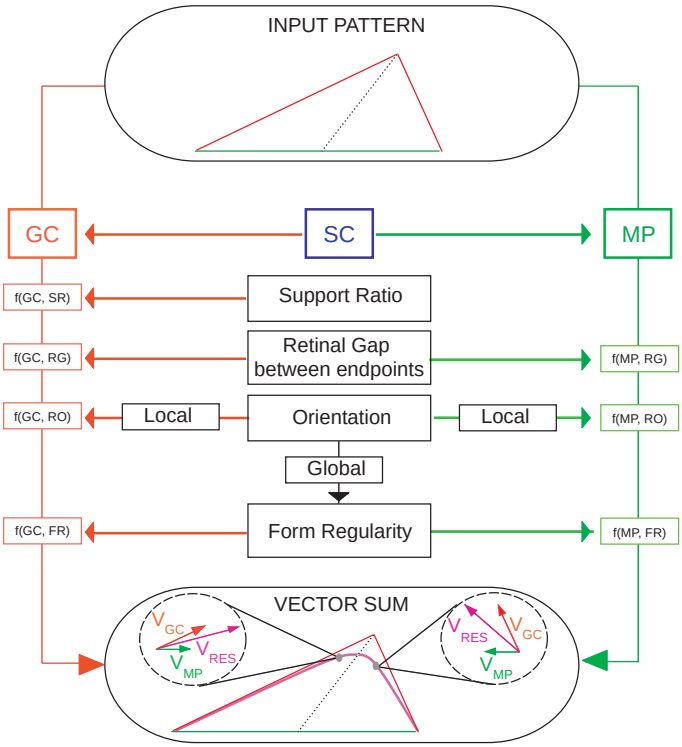

Figure 29. The diagram represents the modulation of unification factors by metrical variables and their interaction. Given an input pattern (top), the model generates GC and MP fields under the SC constraint. Support ratio modulates the GC-magnitude function. Other metrical variables (retinal gap and orientation) modulate both GC- and MP-magnitude functions. GC- and MP-magnitude functions are also modulated by form regularity that mediates a global effect of orientation. The interpolation trajectory (bottom) derives from the chaining of resultants ($V_{RES} = V_{GC} + V_{MP}$).

(c) *Support ratio*. The ratio principle (Shipley & Kellman, 1992b) states that the GC absolute strength depends on the ratio between lengths of the image-specified portion and the total side (including the amodal portion predicted by GC alone). GC becomes stronger as the specified length increases relative to the total length (i.e., when the support ratio is large). However, the MP strength is not influenced by such a ratio, being affected only by the retinal gap between T-junctions. As a consequence, as the image-specified portion increases, the trajectory penetrates more into the GC-MP triangle, making the amodal trajectory more similar to a rectilinear vertex.

We hypothesize that the effects of retinal gap, orientation, and support ratio are not specific to rectilinear fragments with opposite GC-MP angles. Analogous effects should characterize the interpolation of rectilinear fragments with alternate GC-MP angles, as well as the interpolation of curvilinear arcs.

As stated in the introduction, the interpolation of rectilinear fragments with alternate GC-MP angles is partially undetermined because GC extrapolations do not intersect. However, consistent with the context sensitivity of GC and MP fields, we suggest some conjectures.

- As the retinal size of the MP line becomes shorter, the trajectory approximates the MP-line solution.
- As the orientation of T-junction stems approximates vertical or horizontal axes, the trajectory approximates a composite path with abrupt changes of curvature, defined by the two GC lines and the central IR line.
- The same effect is expected when the support ratio increases.

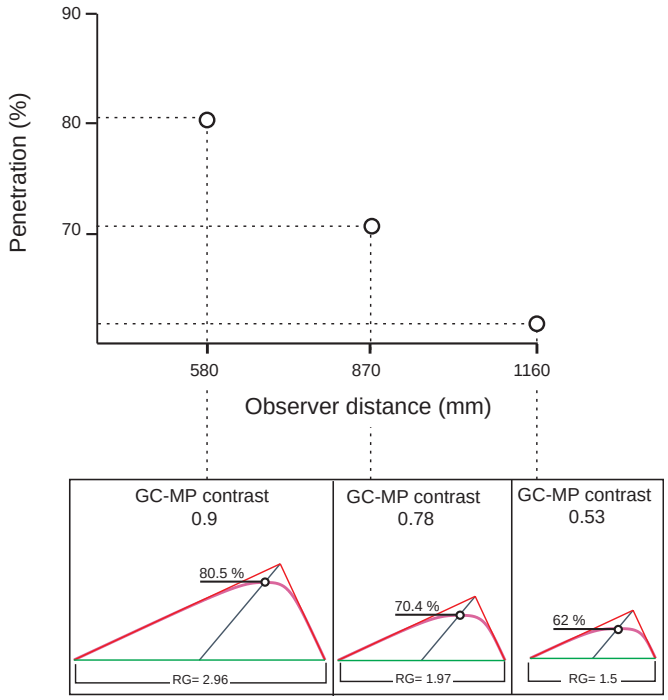

Figure 30. Field model predictions when the retinal gap (RG) between endpoints increases from 1.5 to 3.0 deg and produces a monotonic increase of the amount of penetration. The retinal-gap effect is mediated by a change of the GC-MP contrast value.

Conclusions

We offered a general account of visual interpolation (VI) processes involved in several phenomena. Our field model is new, in the context of other models in the current literature. However, it represents a quantitative implementation of classical unification factors. The interaction of good continuation (GC) and minimal path

(MP) has been modeled according to classical vector field theory.

The field model allowed us to interpolate a broad class of fragment pairs by the chaining of GC- and MP-vector sums. The chaining of resultant vectors gives rise to interpolation trajectories with the following properties: continuity, minimization of inflection points, extended relatability, and context sensitivity. The dynamic VI process implemented in our model is flexible and shows a high predictive power. Furthermore, it provides an explicit formulation of the interaction of classical factors of organization (closure, good continuation, and proximity).

Our field model can embody other organizing factors. For instance, also shape regularity and symmetry might be formalized as weights that modulate GC-MP contrast. However, to account for the effect of nonorthogonal T- and L-junctions, we should add another local factor (different from GC and MP factors). Nonorthogonal T-junctions give rise to Poggendorff-like illusions, consistent with a tendency to normalize angles between occluding and occluded contours. Such a tendency might be implemented in our model as an additional vector oriented along the normal to the T-junction top (TN). In this case, the trajectory should result from the chaining of resultants of three vectors (GC, MP, and TN).

The dynamic approach used in developing our field model provides an alternative way of deriving compatibility criteria. Contrary to geometric criteria typical of the two-stage approach to interpolation, dynamic compatibility criteria are not a priori constraints to the application of an interpolating function. Compatibility measures depend on the distribution of vector fields that model unification factors.

Acknowledgments

This work has been supported by Ministero dell'Università della Ricerca Scientifica e Tecnologica and University of Trieste grants awarded to Walter Gerbino. Authors thank Ennio Mingolla for comments on an earlier draft of this work, Stefano Fantoni for help on the mathematical formalization of the model, and Ted Adelson and two anonymous reviewers for their constructive criticism and useful suggestions.

Commercial relationships: none.

References

Adelson, E. H., & Pentland, A. P. (1996). The perception of shading and reflectance. In D. Knill & W. Richards (Eds.), *Perception as Bayesian Inference* (pp. 409-423). New York: Cambridge University Press.

Birkhoff, G., Burchard, H., & Thomas, D. (1965). Nonlinear interpolation by splines, pseudosplines, and elastica. *General Motors Research Publication* No. 468.

Bregman, A. S. (1981). Asking the "what for" question in auditory perception. In M. Kubovy & J. R. Pomerantz (Eds.), *Perceptual Organization* (pp. 99-118). Hillsdale, NJ: Erlbaum.

Bryant, R., & Griffit, P. (1986). Reduction for constrained varational problems of $\int (K^2/2)ds$. *American Journal of Mathematics, 108,* 525-550.

Buffart, H., Leeuwenberg, E., & Restle, F. (1981). Coding theory of visual pattern completion. *Journal of Experimental Psychology: Human Perception and Performance*, 7, 241-274. [PubMed]

da Pos, O., & Zambianchi, E. (1996). *Visual Illusions and Effects: A Collection*. Milano: Guerini.

Dumais, S. T., & Bradley, D. R. (1976). The effect of illumination level and retinal size on the apparent strength of subjective contours. *Perception & Psychophysics, 19,* 339-345.

Euler, L. (1744). De curvis elasticis. In *Methodus inveniendi leneas curva maximi minimive proprietate gaudentes, sive solutio problematis isoperimetrici lattisimo sensu accepti* Lausannae, *E65*A. O. O. Ser.I. Vol 24.

Fantoni, C. (2000). *Invarianza di scala e interpolazione visiva*. (Scale-invariance and Visual Interpolation). Unpublished master's thesis, University of Trieste, Trieste, Italy.

Fantoni, C., & Gerbino, W. (2001). Probing the amodal completion of asymmetrically occluded angles: A test of interpolation models [Abstract]. *Journal of Vision*, 1(3), 461a, http://journalofvision.org/1/3/461, DOI 10.1167/1.3.461. [Abstract]

Fantoni, C., & Gerbino, W. (2002). A wave-function integration of absolute and relative metric information in visual interpolation [Abstract]. *Journal of Vision*, 2(7), 484a, http://journalofvision.org/2/7/484/, DOI 10.1167/2.7.484. [Abstract]

Fantoni, C., Sgorbissa, F., & Gerbino, W. (2001). Modeling orientation effects in amodal completion [Abstract]. *Perception Supplement*, 30, 20c.

Field, D., Hayes, A., & Hess, R. (1993). Contour integration by the human visual system: Evidence for a local "association field." *Vision Research, 33,* 173-193. [PubMed]

Gerbino, W. (1978). Some observations on the formation of angles in amodal completion. *Italian Journal of Psychology*, *2*, 85-100.

Gerbino, W. (2001). The place of Shepard in the world of perception. *Behavioral and Brain Sciences*, *24*, 669-671.

Gerbino, W., & Fantoni, C. (2000). Amodal completion is not scale-invariant [Abstract]. *Investigative Ophthalmology and Visual Science*, *41*(Suppl. 441), 2335.

Gerbino, W., & Fantoni, C. (2002). Contour polarity and visual interpolation [Abstract]. *Perception Supplement 31*, 152c.

Gerbino, W., & Kanizsa, G. (1987). Can we see constructs? In S. Petry & G. Meyer (Eds.), *The Perception of Illusory Contours* (pp. 246-251). New York: Springer.

Gerbino, W., Sgorbissa, F., & Fantoni, C. (2000). Good continuation and minimal path perturb symmetry judgments in amodal completion [Abstract]. *Abstracts of the Psychonomic Society*, *5*, 85.

Grimson, W. (1981). *From Image to Surfaces: A Computational Study of the Human Early Visual System*. Cambridge: MIT Press.

Grossberg, S., & Mingolla, E. (1985). Neural dynamics of form perception: Boundary completion, illusory figures, and neon color spreading. *Psychological Review*, *92*, 173-211. [PubMed]

Gulick, W. L., & Lawson, R. B. (1976). *Human Stereopsis*. New York: Oxford University Press.

Guy, G., & Medioni, G. (1996). Inferring global perceptual contours from local features. *International Journal of Computer Vision*, *20*, 113-133.

Hatfield, G., & Epstein, W. (1985). The status of the minimum principle in the theoretical analysis of vision. *Psychological Bulletin, 97*, 155-186. [PubMed]

Heitger, F., & von der Heydt, R. (1993). A computational model of neural contour processing: Figure/ground segregation and illusory contours. *Proceedings of the Fourth International Conference on Computer Vision* (pp.32-40). Berlin.

Heitger, F., von der Heydt, R., Peterhans, E., Rosenthaler, L., & Kübler, O. (1998). Simulation of neural contour mechanisms: Representing anomalous contours. *Image and Vision Computing*, *16*, 407-421. [PubMed]

Hon, A. K., Maloney, L. T., & Landy, M. S. (1997). The influence function for visual interpolation. *Human Vision and Electronic Engineering II, Proceedings of the SPIE, 3016*, 409-419.

Horn, B. K. P. (1981). *The Curve of Least Energy*. Cambridge: MIT Press.

Kanizsa, G. (1971). Introduction to the Italian translation of Metzger's *Psychologie*. In *I fondamenti della psicologia della Gestalt*. Firenze: Giunti-Barbera.

Kanizsa, G. (1975). The role of regularity in perceptual organization. In G. B. Flores D'Arcais (Ed.), *Studies in Perception* (pp. 48-66). Firenze: Martello-Giunti.

Kanizsa, G. (1979). *Organization in Vision*. New York: Praeger.

Kanizsa, G., & Gerbino, W. (1982). Amodal completion: Seeing or thinking? In J. Beck (Ed.), *Organization and Representation in Perception*. Hillsdale, NJ: LEA.

Kass, M., Witkin, A., & Terzopolous, D. (1987). Snakes: Active Minimum Energy Seeking Contours. *International Journal of Computer Vision*, *1*, 321-331.

Kellman, P. J. (2000). An update on Gestalt Psychology. In B. Landau, J. Jonides, E. Newport & J. Sabini (Eds.), *Perception, Cognition, and Language: Essays in Honor of Henry and Lila Gleitman* (pp. 157-190). Cambridge: MIT Press.

Kellman, P. J., & Shipley, T. F. (1991). A theory of visual interpolation in object perception. *Cognitive Psychology*, *23*, 141-221. [PubMed]

Kellman, P. J., Guttman, S. E., & Wickens, T. D. (2001). Geometric and neural models of object perception. In T. F. Shipley & P. J. Kellman (Eds.), *From Fragments to Objects: Segmentation and Grouping in Vision*. Oxford, UK: Elsevier Science Publishers.

Kellman, P. J., Shipley, T. F., & Kim, J. (1996). *Local and global effects in object completion: Evidence from a boundary localization paradigm*. Paper presented at the 37th Annual Meeting of the Psychonomics Society, Chicago, IL.

Kellman, P. J., Temesvary, A., Palmer, E. M., & Shipley, T. F. (2000). Separating local and global processes in object perception: Evidence from an edge localization paradigm. *Investigative Ophthalmology and Visual Science*, *41*, 741.

Kelly, F., & Grossberg, S. (2000). Neural dynamics of 3-D surface perception: Figure-ground separation and lightness perception. *Perception and Psychophysics*, *62*, 1596-1619. [PubMed]

Koffka, K. (1935) *Principles of Gestalt Psychology*. New York: Harcourt Brace.

Kovács, I. (1996). Gestalten of today: Early processing of visual contours and surfaces (Review). *Behavioural Brain Research, 82,* 1-11. [PubMed]

Kovács, I., & Julesz, B. (1993). A closed curve is much more than an incomplete one: Effect of closure in figure-ground segmentation. *Proceedings of the National Academy of Science, 90*, 7495-7497. [PubMed]

Love, A. E. H. (1927). *Mathematical theory of elasticity*. Cambridge: University Press.

Markovic, S. (1999). Local and Global factors in the occlusion phenomena: The effect of context complexity [Abstract]. *Perception Supplement*, *28*, B030.

Marr, D. (1982). *Vision*. New York: Freeman.

Metelli, F. (1940). Ricerche sperimentali sulla percezione del movimento. *Rivista di Psicologia*, *36*, 319-370.

Metzger, W. (1954) *Psicologìa.* Buenos Aires: Editorial Nova.

Mumford, D. (1994). Elastica and computer vision. In C. Bajaj (Ed.), *Algebraic Geometry and its Applications* (pp. 491-506). New York: Springer-Verlag.

Musatti, C. L. (1924). Sui fenomeni stereocinetici. *Archivio Italiano di Psicologia*, 3, 105-120.

Musatti, C. L. (1975). Stereokinetic phenomena and their interpretation. In G. B. D'Arcais (Ed.), *Studies in Perception: Festschrift for Fabio Metelli*. Milano: Martello-Giunti.

Nakayama, K., Shimojo, S., & Silverman, G. H. (1989). Stereoscopic depth: Its relation to image fragmentation, grouping, and the recognition of occluded objects. *Perception*, *18*, 55-68. [PubMed]

Sgorbissa, F., & Gerbino, W. (1999). Orientation and amodal completion [Abstract]. *Perception Supplement*, *28*, B137.

Sharon, E., Brandt, A., & Basri, R. (1997). Completion energies and scale. In *Proceedings IEEE Conference on Computer Vision and Pattern Recognition* (pp. 884-890), San Juan, Puerto Rico.

Shipley, T. F., & Kellman, P. J. (Eds.) (2001). *From Fragments to Objects: Segmentation and Grouping in Vision.* Oxford, UK: Elsevier Science Publishers.

Shipley, T. F., & Kellman, P. J. (1992a). Perception of partly occluded objects and illusory figures: Evidence for an identity hypothesis. *Journal of Experimental Psychology: Human Perception and Perfomance*, *18*, 106-120.

Shipley, T. F., & Kellman, P. J. (1992b). Strength of visual interpolation depends on the ratio of physically specified to total edge length. *Perception and Psychophysics*, *52*, 97-106. [PubMed]

Singh, M., & Hoffman, D. (1999) Completing visual contours: The relationship between relatability and minimizing inflections. *Perception & Psychophysics, 61*, 943-951. [PubMed]

Srebotnjak V. (1984). *Orientamento e completamento amodale.* (Orientation and Amodal Completion). Unpublished master's thesis, University of Trieste, Trieste, Italy.

Takeichi, H. (1995). The effect of curvature on visual interpolation. *Perception, 24,* 1011-1020. [PubMed]

Takeichi, H., Nakazawa, H., Murakami, I., & Shimojo, S. (1995). The theory of curvature constraint line for amodal completion. *Perception, 24*, 373-389. [PubMed]

Thompson D'Arcy, W. (1942). *On Growth and Form*. Cambridge: University Press. (Original work published in 1917)

Thornber, K. K., & Williams, L. R. (1996) Analytic solution to stochastic completion fields. *Biological Cybernetics, 75,* 141-151.

Thornber, K. K., & Williams, L. R. (1999). Orientation, scale and discontinuity as emergent properties of illusory contour shape. In M. S. Kearns, S. A. Sola, & D. A. Cohn (Eds.*), Advances in Neural Information Processing Systems 11* (pp. 831-837). Cambridge: MIT Press. [PubMed]

Tse, P. U. (1999a). Volume completion. *Cognitive Psychology*, *39*, 37-68. [Article] [PubMed]

Tse, P. U. (1999b). Complete mergeability and amodal completion. *Acta Psychologica*, *102*, 165-201. [PubMed]

Ullman, S. (1976). Filling-in the gaps: The shape of subjective contours and a model for their generation. *Biological Cybernetics, 25*, 1-6.

Weiss, I. (1988). 3-D shape representation by contours. *Computer Graphics, Vision and Image Processing*, *41*, 80-100.

Wertheimer, M. (1923). Untersuchungen zur lehere von der Gestalt. Psychologische Forschung, 4, 301-350.

Williams, L., & Jacobs, D. W. (1997). Stochastic completion fields: A neural model of illusory contour shape and salience. *Neural Computation 9*, 837-859. [PubMed]

Williams, L. R., & Hanson, A. R. (1996). Perceptual completion of occluded surfaces. *Computer Vision and Image Understanding 64*, 1-20.

Williams, L.R. (1997) Topological reconstruction of a smooth manifold-solid from its occluding contour. *International Journal of Computer Vision, 23*, 93-108.

Witkin, A. P., & Tenenbaum, J. M. (1983). On the role of structure in vision. In J. Beck, B. Hope, and A. Rosenfeld (Eds.), *Human and Machine Vision.* New York: Academic Press.